Advanced Healthcare Materials

ADVANCED HEALTHCARE MATERIALS
www.advhealthmat.de

RESEARCH ARTICLE

Synthetic Antibody Mimetics with ROS-Gated Saccharide Release for Targeted Colitis Therapy

Yan Zhang[1] | Song Li[2] | Qiang Li[1] | Ruiyuan Wang[1] | Yue Sun[1] | Yichun Wang[1] | Xiaomin Yan[1] | Xiaojian Wang[3] | Yufeng Wang[4] | Yadong Xue[5] | Chao Ding[6] | Jianfeng Gong[2] | Lin Ding[1,7] | Huangxian Ju[1]

[1]State Key Laboratory of Analytical Chemistry For Life Science, School of Chemistry and Chemical Engineering, Nanjing University, Nanjing, China | [2]Department of General Surgery, Jinling Hospital, Affiliated Hospital of Medical School, Nanjing University, Nanjing, China | [3]Institute of Advanced Synthesis, School of Chemistry and Molecular Engineering, Nanjing Tech University, Nanjing, China | [4]Department of Chemistry, The University of Hong Kong, Hong Kong, China | [5]Affiliated Jinhua Hospital, Zhejiang University School of Medicine, Jinhua, China | [6]Department of General Surgery, Nanjing Drum Tower Hospital, Affiliated Hospital of Medical School, Nanjing University, Nanjing, China | [7]Chemistry and Biomedicine Innovation Center (ChemBIC), ChemBioMed Interdisciplinary Research Center, Nanjing University, Nanjing, China

Correspondence: Yadong Xue (xueyadong@zju.edu.cn) | Chao Ding (dingchao19910521@126.com) | Jianfeng Gong (gongjianfeng@nju.edu.cn) | Lin Ding (dinglin@nju.edu.cn)

Received: 25 November 2025 | **Revised:** 16 January 2026 | **Accepted:** 28 February 2026

Keywords: IBD | molecularly imprinted polymer | mucus barrier | ROS-responsive release | targeted saccharide delivery

ABSTRACT

Conventional targeted therapies for inflammatory bowel disease (IBD) often rely on unstable biological recognition elements. While molecularly imprinted polymers (MIP) offer robust synthetic alternatives, their utility is limited by an "always-on" binding state: even weak non-specific adsorption can significantly compromise their target-binding capacity. We convert static MIP into reactive oxygen species (ROS)-activated therapeutic actuators by conjugating mannose to transferrin-imprinted MIP via a ROS-cleavable linker. The saccharide acts dually as a therapeutic agent and a protective cloak. It sterically blocks non-specific binding during intestinal transit. At inflammatory sites, elevated ROS levels (higher than in healthy tissue) trigger simultaneous mannose release and activation of high-affinity targeting. This enables precise MIP anchoring to the inflamed epithelium for physical barrier formation and localized microbiome modulation. In murine colitis models, this achieved mucosal healing, mitigated inflammation, and microbiota rebalancing using a mannose equivalent dose of 27.2 mg/kg/d, benchmarking against free mannose and non-responsive MIP controls. This work establishes a generalizable paradigm for targeted recognition and drug delivery in complex physiological environments, paving the way for intelligent, disease-responsive nanomedicines.

1 | Introduction

Inflammatory bowel disease (IBD) [1] presents a formidable challenge for targeted therapy due to the complex and hostile gastrointestinal environment [2]. Current targeting strategies predominantly rely on biological recognition elements (e.g., antibodies, peptides) [3–5]. While effective for systemic injected therapies, these are prone to enzymatic degradation and denaturation in the gastrointestinal tract, severely limiting their utility for oral targeted delivery. Recently, nanocarrier-based drug delivery systems for IBD have flourished [6]. These systems often incorporate modules that respond to environmental stimuli (such as elevated reactive oxygen species (ROS) or dysregulated pH) to release drugs [7]. However, these systems lack robust, specific recognition elements capable of reliably distinguishing diseased tissues.

Molecularly imprinted polymers (MIP) [8] are promising synthetic antibody mimetics that offer superior stability and programmable recognition, positioning them as robust alternatives

to biological agents for targeted applications [9–11]. However, their in vivo efficacy is significantly hampered by an "*always-on*" binding state [12], i.e., target-binding sites remain continuously exposed, allowing unwanted interactions, where even minor non-specific adsorption can markedly compromise target-binding capacity. This limitation is particularly pronounced for oral colon delivery, as the materials must first traverse the highly complex small intestine—a milieu characterized by digestive enzymes, abundant non-specific proteins, and dense microbiota (e.g., trypsin/chymotrypsin, mucins, and *Escherichia coli*) [13–15].

A solution to this "always-on" dilemma lies in designing a molecular switch to control MIP recognition—essentially, a removable cloak for the imprinted cavities. We envisioned that conjugating a therapeutic drug to mask the MIP's binding cavities could prevent off-target binding during transit. Upon stimulus-triggered release, it could also deliver a local regulator. For the payload, sugars act as key molecular mediators orchestrating tripartite host–microbiota–environment interactions [16], positioning gut saccharide intervention as an emerging therapeutic paradigm [17]. They demonstrate "dual-tiered regulation": locally via microbiota remodeling [18, 19] and barrier enhancement [20, 21], and systemically through interorgan axes [22, 23]. However, existing oral sugar protocols require an administration dose of 150–500 mg/d/kg, which incurs systemic side effects [24] while suffering from poor colonic accumulation due to absorptive partitioning in the small intestine [25] and nonspecific dispersion. Therefore, equipping MIPs with a removable "sugar cloak" presents a strategic solution to concurrently address the in vivo targeting challenges for both the MIP carrier and the therapeutic sugar.

Herein, we report a paradigm-shifting approach that transforms MIP from passive recognition elements into intelligent therapeutic actuators through a novel gating strategy (Figure 1a). We conjugate mannose to the surface of transferrin-imprinted nanoparticles [26, 27] via ROS-cleavable boronate ester bonds [28–30]. Mannose was selected because it has reported anti-inflammatory and barrier-protective effects in intestinal inflammation, and can also modulate gut microbial communities [19, 31, 32]. This design creates a sophisticated targeting system where: (1) the saccharide acts as both a therapeutic agent and a protective cloak that sterically blocks the MIP's recognition cavities during transit; (2) at inflammatory sites, elevated ROS levels (10–100-fold higher than in healthy tissue) [33] trigger saccharide release, simultaneously unmasking the high-affinity targeting cavities and delivering the therapeutic payload; and (3) the exposed MIP specifically anchors to the inflamed epithelium to form protective barriers.

Compared with previous MIP-based oral systems, this disease-activated gating strategy addresses the "always-on" limitation by minimizing nonspecific interactions during intestinal transit, thereby improving effective in vivo recognition in inflamed, ROS-rich tissue. Aided by an enteric coating to resist gastric acid, our oral nanoprobe achieves unprecedented targeting specificity in murine colitis models (Figure 1b). It addresses the multifactorial pathology of IBD by restoring mucosal integrity, rebalancing microbial communities, and suppressing inflammatory cytokines, outperforming conventional high-dose saccharide regimens through a low-dose, targeted intervention. Our work establishes MIP-based artificial antibodies as a generalizable platform for targeted drug delivery in environments where biological ligands fail, opening new avenues for treating IBD and other inflammatory diseases with intelligent, disease-responsive therapeutic systems.

2 | Results and Discussion

2.1 | Construction of Transferrin-Targeting Synthetic Antibody Mimetics

Molecularly imprinted polymers bind targets with high affinity through size complementarity and multivalent interactions [9, 10], while their surface functional groups permit further chemical modification. We therefore selected transferrin (Tf)—a protein markedly enriched on inflamed colonic epithelia and a key molecular target for intervention [26, 27]—as a template to engineer MIP that serve as synthetic antibody mimetics by specifically recognizing inflammatory sites in the colon. Tf enrichment is associated with inflammation-driven increases in mucosal transferrin exposure and epithelial transferrin receptor (TfR/CD71/TFRC) expression, which together enhance local Tf engagement [27, 2, 34].

Figure 2a outlines the synthetic procedure. Fluorescein isothiocyanate (FITC)-doped silica nanoparticles (FITC-SiO_2; 100–120 nm diameter, ζ-potential: -37.5 ± 0.4 mV) served as fluorescent tracing cores (Figure 2b,c). The Tf template was immobilized onto these cores using 4-carboxyphenylboronic acid as the linker (Figure S1). A surface-imprinting polymerization was then carried out using 2-aminopropyl methacrylate (2-AM) as the functional monomer and *N*,*N*'-methylene bisacrylamide (MBA) as the crosslinker. Subsequent acid treatment removed the Tf templates, generating specific recognition cavities and yielding the final MIP nanoparticles. The resulting MIP featured a ~15-nm-thick imprint layer and exhibited a ζ-potential shift to +45.5 ± 0.6 mV (Figure 2b,c), confirming successful polymer coating.

The Tf-specific binding capability of MIP was systematically evaluated in solution, in vitro, and in vivo. In a solution containing 0.4 mg mL^{-1} Tf, MIP exhibited a 3.1-fold adsorption capacity (43.3 ± 1.7 μg mg^{-1}, $p < 0.0001$) compared to non-imprinted polymers (NIP) (Figure 2d,e). Selectivity assays against control proteins, including mucin 2 (MUC2, dominant intestinal mucin) [35, 36], bovine serum albumin (BSA) and albumin (ALB), confirmed the preferential binding of MIP to Tf (Figure 2f). Although adsorption of control proteins by MIP accounted for no more than 15.8% (for ALB) of its total capacity, it still led to a substantial decrease in subsequent Tf binding (Figure S2). As the molecular weight of control proteins decreased, this effect became more pronounced. We attribute this to cavity occlusion: smaller proteins can more readily penetrate or lodge within the imprinted cavities (or their entrances), blocking Tf access even at low overall adsorption. For ALB, pre-adsorption resulted in an 81.1% reduction in Tf adsorption. These data suggest that even limited non-specific adsorption can occlude the cavities and hinder target access, thus highlighting the necessity of a switchable targeting strategy for oral delivery to minimize off-target interactions in the complex intestinal environment. For in vitro validation, Tf-functionalized glass slides were used to mimic inflamed epithelia,

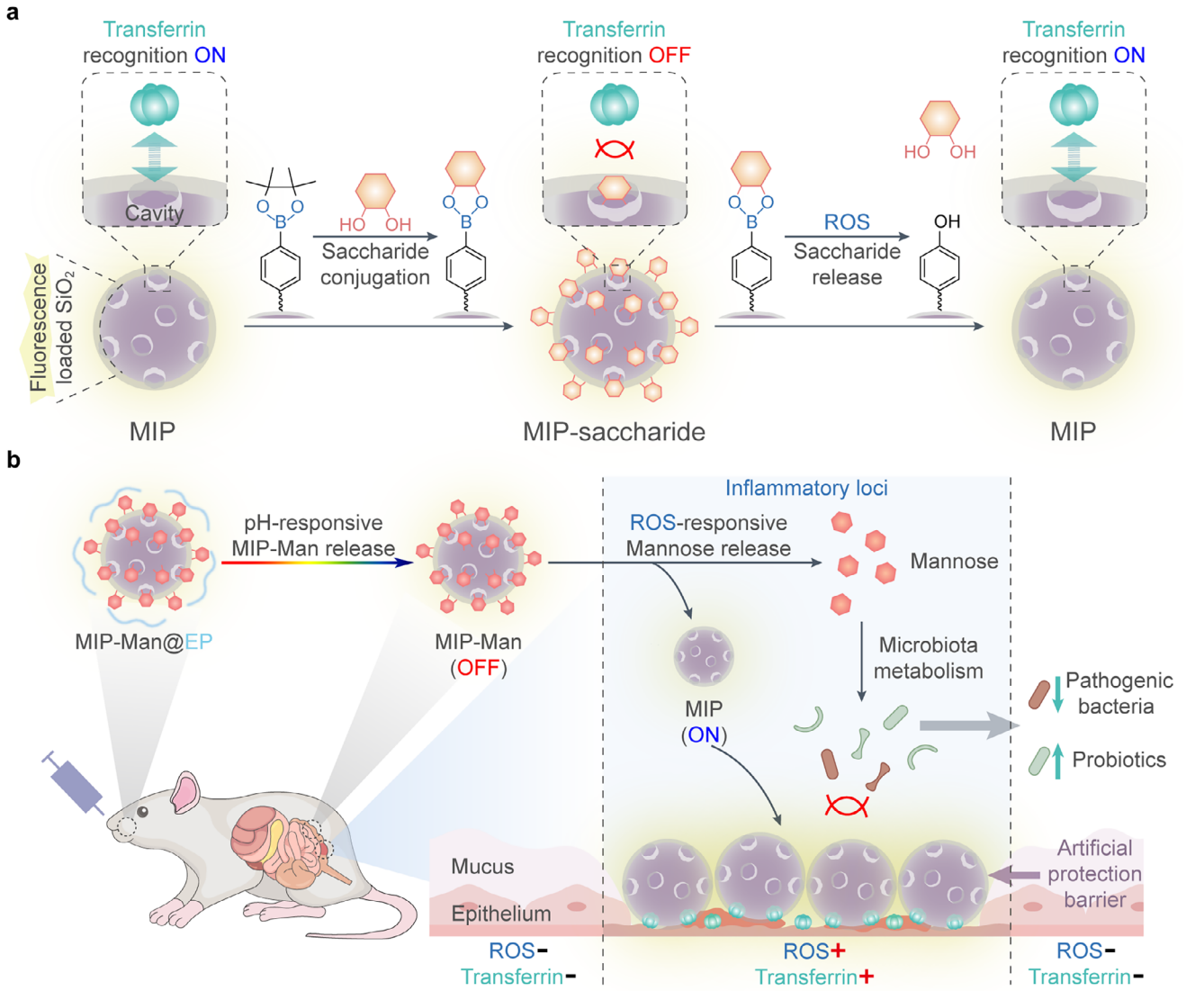

FIGURE 1 | Fluorescently doped, saccharide-conjugated molecularly imprinted polymers (MIP) for targeted colitis management. (a) Schematic of the gating strategy. A transferrin-imprinted MIP was synthesized using fluorescently doped SiO_2 as the carrier. Saccharides were conjugated via borate linkages to sterically block the binding cavities, generating MIP-saccharide. Subsequent ROS-triggered saccharide release unblocks the cavities and reactivates target binding. (b) In vivo imaging and treatment in a murine colitis model. MIP-mannose (MIP-Man) was encapsulated within an Eudragit S100 (ES100)/poly(lactic-co-glycolic acid) (PLGA) composite (EP), forming the oral probe MIP-Man@EP. The probe remains stable under gastric conditions but releases MIP-Man in the intestine. At inflamed colon sites (characterized by elevated ROS and epithelial-associated transferrin), ROS-triggered mannose release allows MIP binding to transferrin, forming a protective physical barrier and simultaneously reprogramming the dysbiotic microbiota.

while MUC2-coated (healthy epithelium mimic) and BSA-coated slides served as controls [26]. Fluorescence imaging confirmed stronger MIP binding to Tf-presenting surfaces relative to controls (Figure S3).

We further evaluated the targeting efficacy in a DSS-induced murine colitis model (2.5% DSS in drinking water for 7 days), which is clinically relevant to human ulcerative colitis (Figure 2g–k). MIP (or NIP, 40 mg mL^{-1}) was administered 4 h intracolonically after the last DSS treatment. Following intracolonic administration, MIP accumulation in inflamed tissues was 24.5-fold greater than in tissues from healthy mice (Figure 2h,j), demonstrating a strong inflammation-targeting capability. In contrast, NIP showed negligible accumulation in both healthy and inflamed tissues (Figure 2i,k), confirming that the observed specificity is indeed conferred by the imprinted cavities. Within inflamed colons, the accumulation of MIP was 13.0-fold higher than that of NIP (Figure 2j,k). This enrichment ratio substantially exceeds the fold enrichment reported in the literature for systemically administered antibodies: in that study, the accumulation of an anti-extradomain A antibody (F8-VEGFC) over its isotype control in a similar DSS colitis model was 1.5-fold [37]. The superior targeting performance of our MIP likely originates from their polyvalent binding avidity and inherent resistance to proteases. Collectively, these results establish that our synthetic antibody mimetic possesses excellent specific binding within inflamed colons, highlighting its potential for oral targeted delivery.

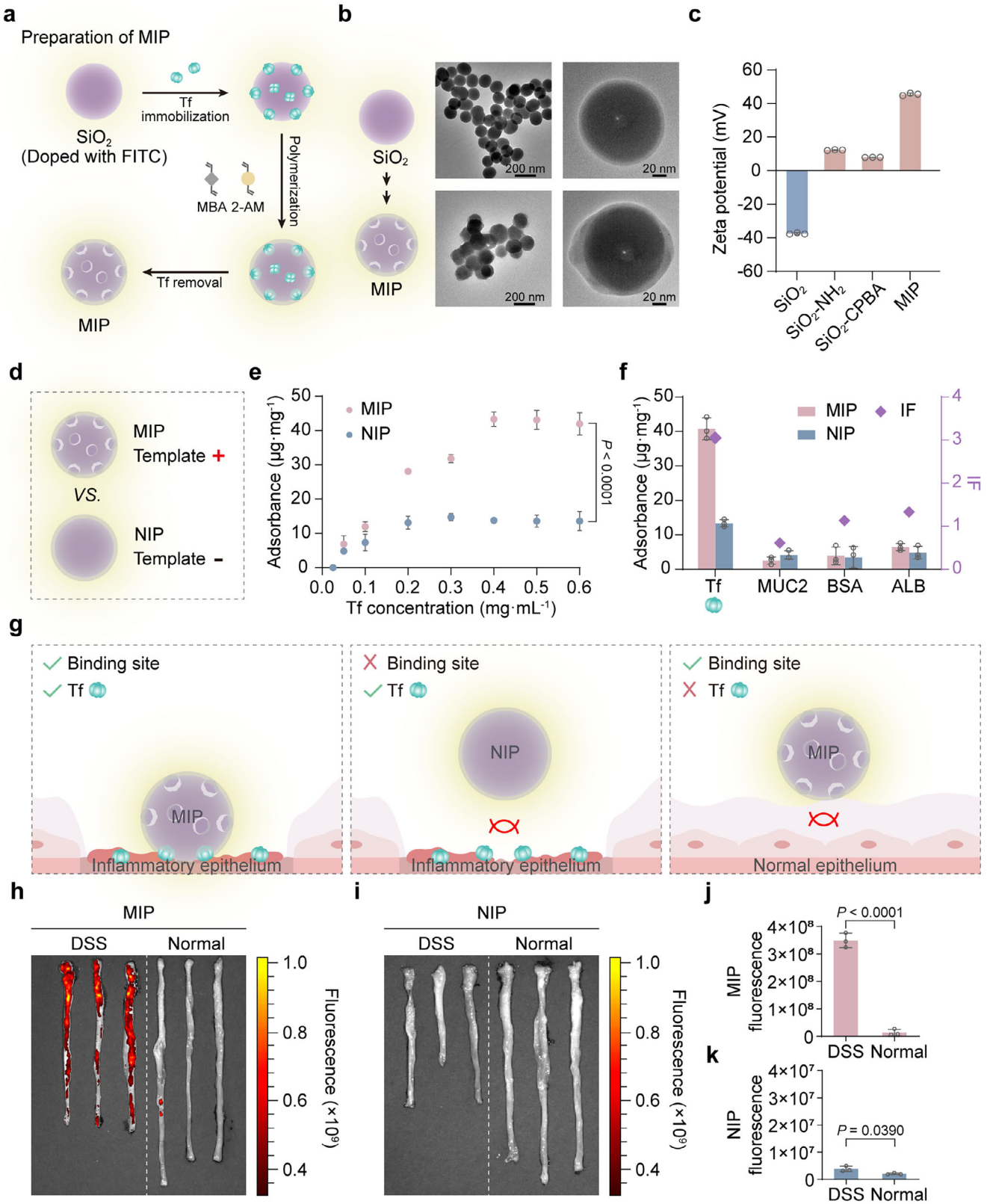

FIGURE 2 | Construction and specific recognition of transferrin-targeting MIP. (a) Schematic of the synthesis procedure of transferrin (Tf)-imprinted MIP using FITC-doped SiO_2 as the core. (b) Transmission electron microscopy (TEM) images of the SiO_2 core (top) and the resulting MIP (bottom). The MIP image reveals a uniform polymer layer on the surface. Scale bars: 200 nm (left) and 20 nm (right). (c) Zeta potential measurements of the synthetic intermediates and the final MIP. (d) Schematic illustration comparing MIP with the nanoparticles without imprinted polymers (NIP). (e) Binding isotherms of MIP and NIP after 2 h incubation in Tf solutions at 37°C. Data show the amount of Tf adsorbed (μg per mg of nanoparticles). (f) Binding selectivity of MIP toward transferrin (Tf) vs. control proteins (MUC2, BSA, ALB). The imprinting factor (IF) is calculated as the ratio of MIP adsorption to NIP adsorption. g) Diagram depicting the proposed binding mechanisms of MIP and NIP at the normal vs. inflamed intestinal epithelium,

2.2 | Modulation of MIP Binding with a Saccharide-Based Gating Strategy

After obtaining MIP with specific targeting capability, we sought to minimize its non-specific adsorption during delivery by blocking the MIP cavities with a removable saccharide (as a therapeutics) cloak. We first established the conjugation and release chemistry using a library of model saccharides, including three monosaccharides (glucose, galactose, mannose), one disaccharide (lactose), and one polysaccharide (mannan). We employed ROS-cleavable boronate ester bonds to conjugate and subsequently release saccharides (Figure 3a; Figure S4). The successful formation of phenylboronic acid-saccharide complexes and the subsequent ROS-triggered saccharide release was confirmed by ^{1}H NMR for all saccharides tested (Figure 3b; Figures S5–S9). These results confirm the robustness and universality of ROS-triggered saccharide release via boronate ester chemistry, providing a versatile toolbox for diverse saccharide therapeutics.

With the chemical feasibility established, we integrated this programmable release mechanism with our synthetic antibody mimetics. This integration not only creates an intelligent nanoplatform but also achieves a dual-purpose design: the conjugated saccharide acts simultaneously as a protective cloak and a releasable therapeutic. Saccharides were covalently conjugated to the amine groups on MIP via a nitrophenyl-functionalized phenylboronic acid pinacol ester [38] (Figure 3c; Figures S10–S12), creating an interface that displays saccharides in a multivalent manner. Taking mannose grafting as an example, the morphology of MIP-Man remained unchanged after conjugation (Figure 3d). Successful grafting was confirmed by the reversal of surface charge to -29.3 ± 1.3 mV. The negative surface potential is favorable for subsequent targeting to the positively charged inflamed epithelium. Quantitatively, an exhaustive oxidative cleavage assay (20 mM H_2O_2) indicated an initial mannose grafting density of 39.0 ± 3.7 μg mg^{-1} nanoparticles (Supporting Information). Critically, this conjugation sterically blocked the MIP's cavities, reducing transferrin binding by 90.0% and 93.8% for MIP-Man and MIP-Mannan, respectively (Figure 3e,f), indicating near-complete blockade.

We then demonstrated H_2O_2-triggered saccharide release. High performance liquid chromatography (HPLC) quantification confirmed H_2O_2 concentration- and time-dependent release of mannose from MIP-Man (Figure S13). Under simulated colitis conditions (500 μM H_2O_2 [39, 40], 4 h), the release capacities followed the order: mannan (75.7 μg mg^{-1}) > lactose (38.4 μg mg^{-1}) > mannose (34.0 μg mg^{-1}) > galactose (29.4 μg mg^{-1}) > glucose (15.6 μg mg^{-1}) (Figure 3g), demonstrating broad applicability. Notably, the released mannose under simulated colitis conditions (34.0 μg mg^{-1}) corresponds to ~87% of the initial grafted amount (39.0 μg mg^{-1}), indicating efficient ROS-responsive de-gating in an inflammatory milieu. Most critically, H_2O_2-triggered saccharide liberation concurrently restored the targeting function of the synthetic antibody mimetics, as evidenced by a significant recovery of transferrin binding post-release (64.5% for MIP-Man; 63.0% for MIP-Mannan; Figure 3f). Despite the efficient mannose release (~87% under simulated colitis conditions), Tf binding recovered only to ~64.5%, suggesting a non-linear "de-gating–function" relationship. We speculate that a small residual fraction of mannose can disproportionately suppress target binding by persisting at cavity entrances or high-affinity imprinted sites, thereby occluding Tf access. This interpretation is consistent with our selectivity/pre-adsorption assays (Figure S2), where even limited pre-adsorption of non-target proteins (≤15.8% of total adsorption capacity) markedly reduced subsequent Tf binding (e.g., an 81.1% decrease after ALB pre-adsorption), indicating that partial occupancy of cavities/entrances can strongly impede Tf recognition. Importantly, the measurable recovery confirms the intended ROS-responsive gating and reactivation of targeting. Collectively, these data establish an intelligent MIP nanoplatform in which a disease biomarker (ROS) triggers a therapeutics release that simultaneously unlocks the targeting function.

2.3 | In Vivo Targeting of Orally Administered Saccharide-Conjugated MIP

To enable robust oral delivery and precise colonic release, we encapsulated MIP-Man with pH-responsive Eudragit S100 (ES100, insoluble in acid but soluble at neutral pH) [41] and biodegradable PLGA [42], forming MIP-Man@EP nanoprobes (Figure 4a). The ES100 coating ensures targeted dissolution in the neutral colonic environment, while the PLGA matrix undergoes controlled erosion to enable sustained drug release. TEM confirmed intact coatings after 4-h exposure to pH 2.0, whereas complete dissolution occurred at pH 7.4 (Figure 4b). HPLC analysis revealed mannose release exclusively in pH 7.4 buffer containing H_2O_2 (Figure 4c), with release levels matching uncoated MIP-Man (Figure 3g). Probes pretreated at pH 2.0 for 4–16 h maintained responsive mannose release in pH 7.4 buffer containing H_2O_2 (Figure S14), demonstrating ≥16-h gastric stability. Critically, Tf binding capacity recovered post-release (Figure 4d), comparable to the uncoated MIP-Man after release, confirming preservation of molecular recognition sites. These data establish the EP-coating's functionality: gastric protection without compromising inflammatory microenvironment responsiveness.

We next evaluated the binding capacity of MIP-Man@EP to transferrin (Tf) under conditions mimicking the oral delivery route, using simulated gastric (SGF, pH 2.0), intestinal (SIF, pH 6.8), and colonic fluids (SCF, pH 7.4). In the absence of the mannose cloak, MIP@EP after sequential incubation in SGF (4 h) and SIF (2 h) exhibited significantly stronger nonspecific adsorption (10.4 ± 0.9 mg mL^{-1}) compared to MIP-Man@EP (2.87

where Tf is overexpressed. (h,i) Ex vivo fluorescence images of colons from healthy (Normal) and DSS-induced colitic (DSS) mice, 4 h after intracolonic administration of MIP (h) or NIP (i). (j,k) Quantification of the fluorescence intensity shown in (h) and (i) for MIP (j) and NIP (k) groups, respectively. Data in (b) are representative of three independent experiments with similar results. Data in (c,e,f) are presented as mean ± SD ($n = 3$ independent experiments). Data in (h–k) are representative of two independent experiments ($n = 3$ biologically independent animals); Data in (j,k) are presented as mean ± SD ($n = 3$ biologically independent animals). p values were determined using two-sided Student's t-test.

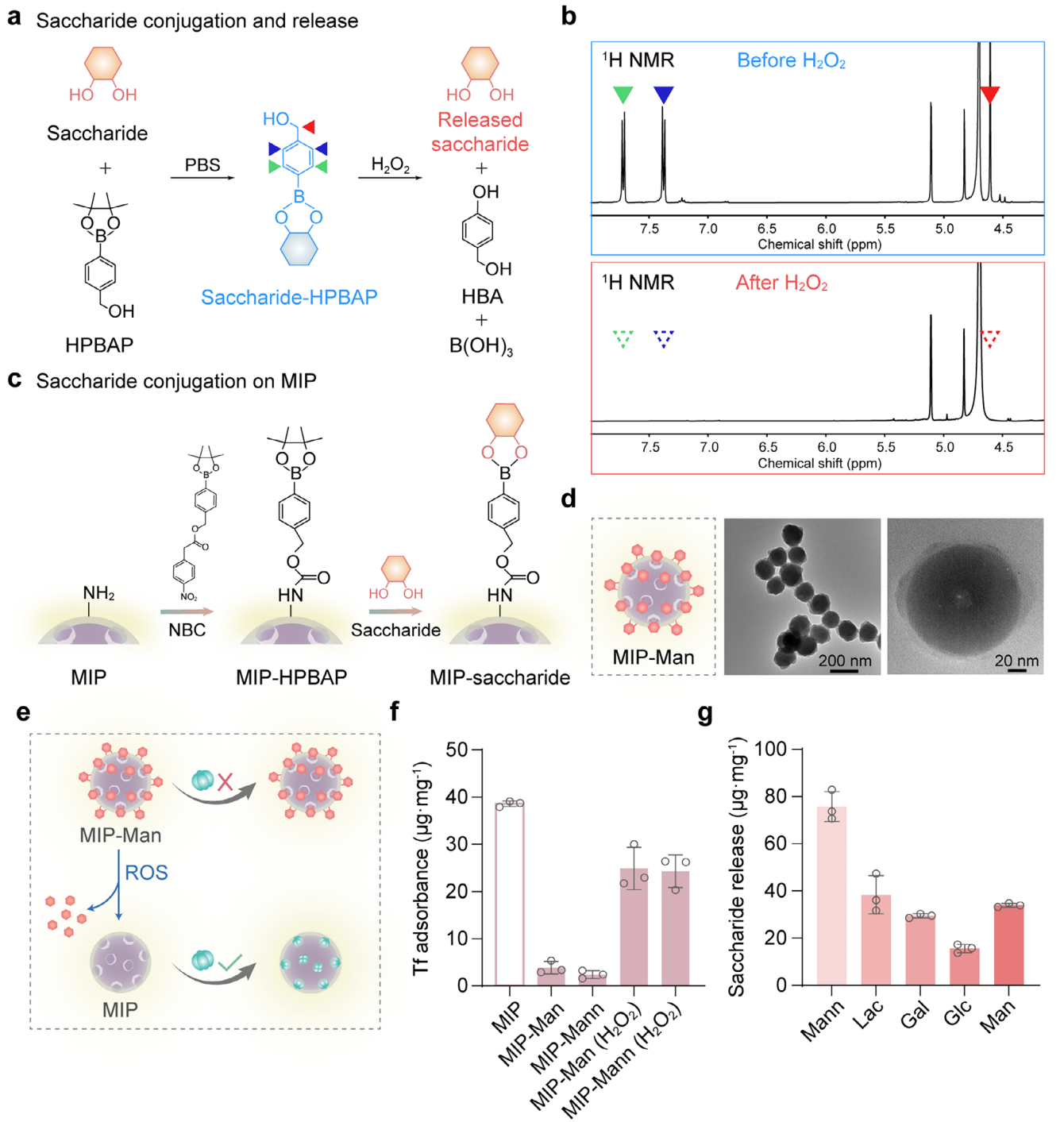

FIGURE 3 | Equipping MIP with the saccharide-based gating module. (a) Saccharide conjugation and release mechanism. Saccharides react with 4-(hydroxymethyl)phenylboronic acid pinacol ester (HPBAP) to form saccharide-HPBAP. H_2O_2-triggered cleavage of the boronate ester bond releases saccharides, 4-hydroxybenzyl alcohol (HBA), and boric acid. (b) ^{1}H NMR spectra demonstrating H_2O_2-triggered mannose release (related to Figure S5). (c) Schematic of saccharide conjugation to MIP. (d) TEM images of MIP-Man. MIP-Man shows uniform polymer surface layers, unchanged after saccharide conjugation. Scale bars: 200 nm (left), 20 nm (right). (e) ROS-triggered mannose release restores MIP recognition toward Tf. (f) Tf adsorption of MIP-Man and MIP-Mannan (μg Tf per mg nanoparticles) before/after H_2O_2 treatment (0.5 mM, 4 h, 37°C). (g) Saccharides released from different MIP-saccharides (μg saccharide per mg nanoparticles) post-H_2O_2 treatment (0.5 mM, 4 h, 37°C). Data in (b,d) are representative of three independent experiments with similar results. Data in (f,g) are presented as mean ± SD ($n = 3$ independent experiments).

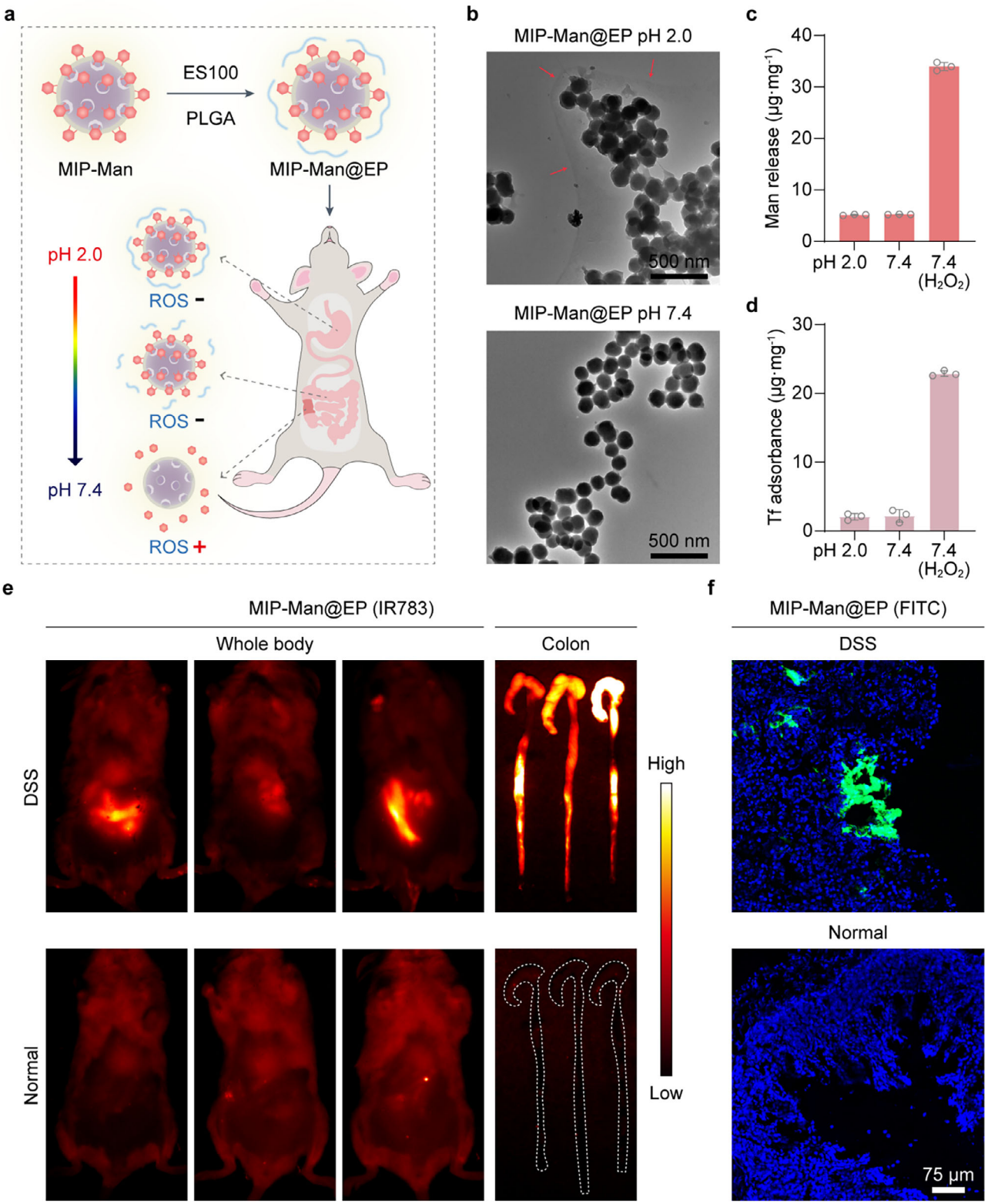

FIGURE 4 | Gastrointestinal delivery and responsive activation of MIP-Man@EP. (a) Schematic of MIP-Man encapsulation in ES100/PLGA composite (EP) for oral delivery, enabling pH-responsive EP dissolution and ROS-triggered mannose release. (b) TEM images of MIP-Man@EP after 4 h incubation in PBS buffers (pH 2.0 or 7.4). Red arrows indicate the EP interface (upper). Scale bars, 500 nm. (c,d) Mannose release (c, μg mannose per mg nanoparticles) and Tf binding capacity (d, μg Tf per mg nanoparticles) of MIP-Man@EP in: pH 2.0 PBS, pH 7.4 PBS, and pH 7.4 PBS containing 0.5 mM H_2O_2 (37°C, 4 h). (e) In vivo binding of IR783-doped MIP-Man@EP to intestinal tracts of healthy (Normal) and colitic (DSS) mice. Whole-body and ex vivo colon fluorescence imaging 22 h post-oral gavage. (f) CLSM images of colon sections 24 h post-administration of FITC-doped MIP-Man@EP. Scale bar, 75 μm. Data in (b) are representative of three independent experiments with similar results. Data in (c,d) are presented as mean ± SD ($n = 3$ independent experiments). Data in (e,f) are presented as a representative of two independent experiments ($n = 3$ biologically independent animals).

± 1.8 mg mL^{-1}) (Figure S15a). This effect was largely attributed to adsorption of protease molecules present in SIF [13, 14]. Although nonspecific adsorption accounted for only 25.5% of the total adsorption capacity, it markedly reduced subsequent Tf binding in PBS or SCF containing 180 μM H_2O_2 and 0.5 mg mL^{-1} transferrin (4 h), which decreased to only 35.9% and 29.0%, respectively, of the Tf adsorption observed with MIP-Man@EP (Figure S15b). These results confirm that the sugar cloak effectively shields MIP from nonspecific adsorption, thereby preserving targeting capacity during gastrointestinal transit and maintaining binding function prior to reaching the target site.

We next assessed the in vivo targeting capability of the MIP-Man@EP nanoprobe via oral gavage. We administered NIR-labeled MIP-Man@EP (IR783) to healthy and DSS-induced colitic mice (nanoparticle dose: 800 mg/kg/day; mannose-equivalent dose: 27.2 mg/kg/day, Supporting Information). Following administration, gastrointestinal fluorescence was observed in both healthy and colitic mice at 4 h. Whereas signals cleared in healthy intestines by 16 h, intense fluorescence persisted in inflamed colons for 22–24 h (Figure 4e; Figure S16), indicating inflammation-specific retention and protection from clearance. Quantitative analysis revealed mean fluorescence intensity (MFI) of 96.5 ± 21.2 a.u. in inflamed colons, compared to 4.3 ± 0.5 a.u. in healthy tissues, representing a 22.4-fold increase. This demonstrates that MIP-Man@EP (IR783) successfully navigates the GI tract, sheds its EP coating in the neutral colon, and responds to elevated ROS levels at inflamed sites to release mannose and activate targeting. The prolonged residence also reflects MIP's strong multivalent interactions and protease resistance. Comparative analysis at 24 h post-administration revealed selective accumulation of MIP-Man@EP (IR783) in colitic tissues vs. control NIP-Man@EP (IR783) (Figure S17), confirming molecular imprinting-mediated targeting. This aligns with prior intracolonic MIP administration results (Figure 2h–k). Further validation using orally delivered MIP-Man@EP (FITC) (Figure S18) demonstrated perilesional enrichment along ulcer margins in inflamed colon sections (Figure 4f), with negligible healthy tissue signal, confirming in vivo targeting specificity to pathological sites.

2.4 | Assessment of the Biosafety of Mannose-Conjugated Synthetic Antibody Mimetics

To evaluate the in vivo biosafety of MIP-Man@EP, healthy mice were orally administered MIP-Man@EP for 10 consecutive days using the same regimen as in the delivery studies. Splenocytes were harvested and analyzed by flow cytometry to assess potential immune activation [43]. Compared with the PBS-treated group, MIP-Man@EP-treated mice showed no significant changes in frequencies of total leukocyte as well as major immune cell populations (Figure S19). Consistently, histopathological examination of major organs (heart, liver, spleen, lung, and kidney) revealed preserved tissue architecture without overt pathological lesions in the MIP-Man@EP group, comparable to PBS-treated controls (Figure S20). Serum biochemistry further showed that liver-function markers (ALT, AST, ALP), kidney-function markers (CREA-S, UA), and albumin (ALB) remained within normal ranges and were not significantly different from those in control mice. Collectively, these results indicate that repeated oral administration of MIP-Man@EP did not elicit overt systemic immune activation or detectable organ toxicity under the tested conditions.

We note that the lesion-shielding "physical barrier" is designed to be focal and microscopic, arising from reversible multivalent anchoring at inflamed epithelial microdomains rather than a continuous coating of the mucosa; thus, it is unlikely to measurably compromise global absorptive function. In addition, any surface-associated particles are expected to be transient because intestinal epithelial turnover with luminal shedding occurs over ~3–5 days [44] and is accompanied by mucus turnover and peristaltic clearance [45, 46]. While our current data do not suggest overt malabsorption, comprehensive preclinical studies will be important to directly quantify long-term retention and intestinal function, such as nutrient absorption assays and gastrointestinal physiological readouts.

2.5 | Mannose-Conjugated Synthetic Antibody Mimetics Exhibit Therapeutic Efficacy in Colonic Inflammation

We next evaluated the therapeutic efficacy of MIP-Man@EP in DSS-induced murine colitis. Following successful disease induction with 2.5% DSS in drinking water (days 0–6), inflamed mice were randomized into five treatment groups (n = 5 per group) receiving daily oral gavage from day 3 for eight consecutive days: PBS (negative control), free mannose (Man group), MIP@EP (MIP core with enteric coating), NIP-Man@EP (non-imprinted control), and MIP-Man@EP (experimental), alongside healthy normal controls (Figure 5a). Terminal analysis at day 11 revealed superior therapeutic outcomes for the MIP-Man@EP cohort. This group exhibited the most significant weight recovery (100.6% ± 3.6% vs. 73.0%–75.8% in controls; Figure 5b), the lowest disease activity index (DAI = 0.6 ± 0.4 vs. 2.7–3.1; Figure 5c), and colon length restoration comparable to healthy mice (6.3 ± 0.5 cm vs. 4.4–4.8 cm in controls; Figure 5d; Figure S21). Histopathological analysis showed near-complete crypt architecture preservation in MIP-Man@EP-treated mice (Figure 5e), contrasting sharply with epithelial damage and crypt destruction in control groups. Blinded histological scoring (total score 0–12; based on crypt damage [0–6] and inflammatory cell infiltration [0–6]; see Experimental Section/Methods for details) confirmed these findings, with the experimental group approaching healthy tissue metrics (Figure S22). The marked therapeutic superiority over comparator groups—particularly compared to MIP@EP (barrier formation without saccharide release) and NIP-Man@EP (saccharide delivery without barrier formation)—suggests the essential synergistic action of inflammation-targeted barrier formation and mannose release. This synergy likely arises from the physical barrier that shields the mucosa and from the locally concentrated mannose, which modulates the microbiome and inflammatory response, thereby creating a self-reinforcing cycle of repair.

2.6 | Mannose-Conjugated Synthetic Antibody Mimetics Promote Barrier Restoration and Inflammation Resolution

We next dissected therapeutic contributions through molecular and microbiota-level analyses. At the molecular level, MIP-Man@EP demonstrated superior intestinal barrier restorative

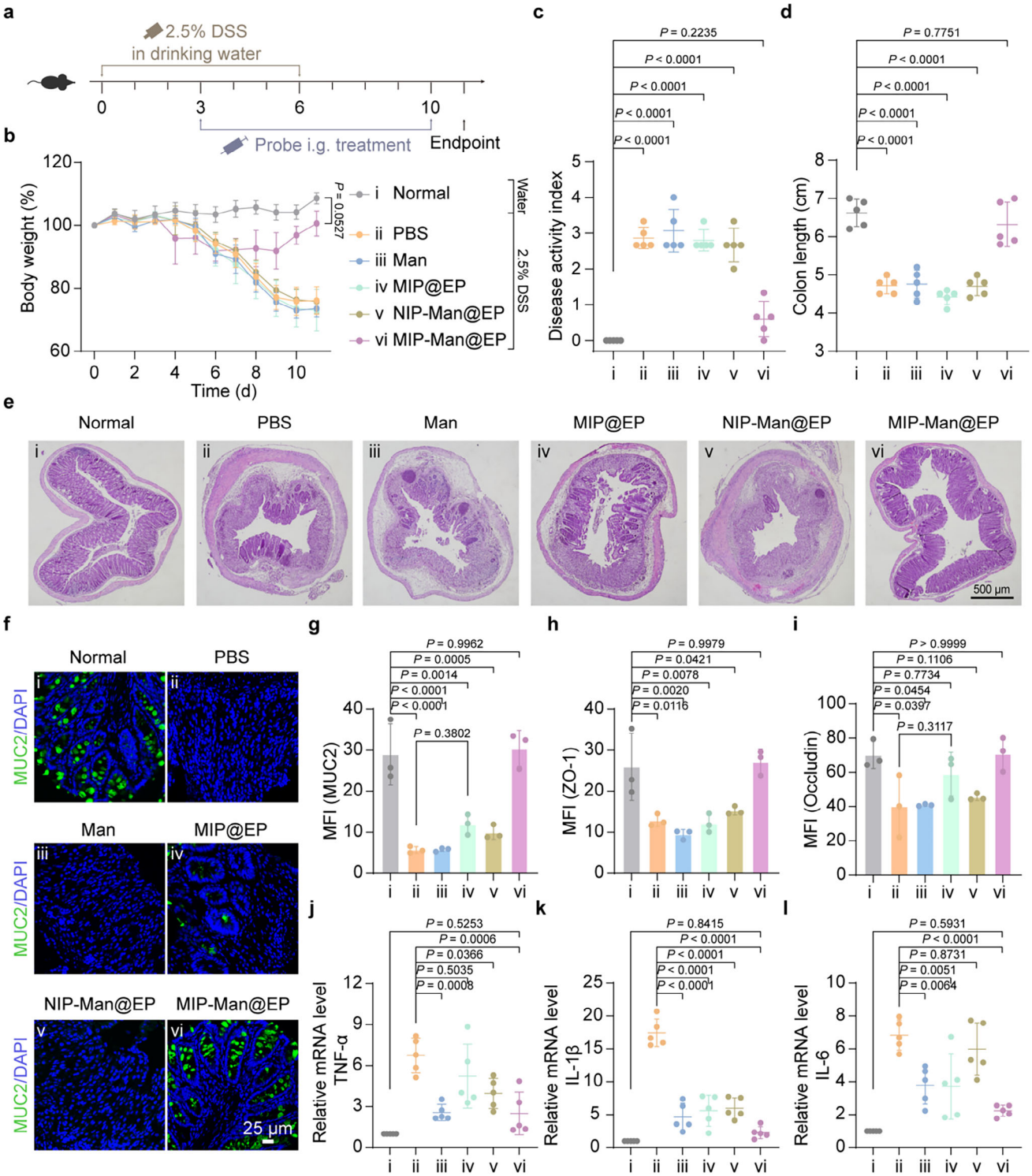

FIGURE 5 | Therapeutic efficacy of MIP-Man@EP in DSS-induced murine colitis. (a) Treatment timeline. Mice were randomly divided into six groups: the normal group (i, Normal) was given regular water, while the other five groups received 2.5% DSS in drinking water for 6 days to induce colitis. From day 3 to day 10, the following solutions were administered via daily oral gavages: (ii) PBS, (iii) Man, (iv) MIP@EP, (v) NIP-Man@EP, and (vi) MIP-Man@EP. Study endpoint: day 11. (b) Relative body weight change during treatment. Initial weight = 100%. (c) Disease activity index (DAI) scores on day 11. (d) Colon lengths at endpoint (related to Figure S21). (e) H and E-stained colon sections. Scale bar, 500 μm (related to Figure S22). (f) MUC2 immunohistochemistry. Scale bar, 25 μm. (g–i) Quantitative analysis of mean fluorescence intensity (MFI) of MUC2 (g), ZO-1 (h), and occludin (i) (from f; Figure S23). (j–l) Relative colonic mRNA levels of TNF-α (j), IL-1β (k), IL-6 (l). Data in (b–l) are representative of two independent experiments. Data in (b–d and j–l) are presented as mean ± SD ($n = 5$ biologically independent animals). Data in (g–i) are presented as mean ± SD ($n = 3$ biologically independent animals (randomly selected from each group of Figure 5b)). p values were determined by ordinary one-way ANOVA with Tukey's multiple comparisons test.

effects vs. control probes. MUC2, a critical structural component of the colonic mucus layer [35], is depleted during goblet cell dysfunction in colitis [47]. Intense crypt-localized MUC2 fluorescence in MIP-Man@EP-treated mice—comparable to healthy controls—indicated restored goblet cell function and enhanced mucus secretion (Figure 5f,g). While control groups showed minimal MUC2 signals, moderate MUC2 recovery in MIP@EP mice suggested targeted MIP binding alone aids mucosal repair. Furthermore, MIP-Man@EP normalized the distribution and expression of tight junction proteins ZO-1 and occludin—essential for barrier integrity [48, 49]—to levels indistinguishable from healthy tissues (quantified via MFI of immunofluorescence; Figure 5h,I; Figure S23). Intermediate occludin recovery in MIP@EP mice further supported reparative role of MIP binding.

Pro-inflammatory cytokine imbalance characterizes IBD progression [50]. Quantitative PCR analysis (normalized to GAPDH) revealed that MIP-Man@EP reduced TNF-α, IL-1β, and IL-6 mRNA to baseline (Figure 5j–l), signifying potent anti-inflammatory activity. Comparator groups showed partial efficacy: Free mannose significantly reduced TNF-α and IL-1β with modest IL-6 reduction; NIP-Man@EP reduced TNF-α and IL-1β. We thus infer that mannose release dominates MIP-Man@EP's anti-inflammatory activity, consistent with prior reports [51]. To further substantiate this inference, we performed an in vitro comparison using an LPS-stimulated Caco2 inflammation model. Four groups were tested: untreated cells, free mannose, mannose-free MIP (targeting scaffold only), and a physical mixture of mannose-free MIP with free mannose (at the same mannose dose). Free mannose and the physical mixture similarly suppressed the secretion of pro-inflammatory cytokines (IL-2 and TNF-α), whereas the mannose-free MIP alone showed no detectable anti-inflammatory effect (Figure S24). These data support the conclusion that mannose release is the major driver of the observed immunomodulation.

2.7 | Mannose-Conjugated Synthetic Antibody Mimetics Restore Microbial Homeostasis in Colitis

Gut microbiota dysbiosis—a hallmark of inflammatory bowel disease (IBD)—drives disease progression through enhanced immune activation, epithelial dysfunction, and compromised barrier integrity [52, 53]. 16S rDNA sequencing revealed that MIP-Man@EP restored α-diversity (Shannon index, Faith's phylogenetic diversity (Faith's PD)) to near-healthy levels, outperforming all comparators (Figure 6a; Figure S25a). β-Diversity analysis (Jaccard/Unweighted UniFrac metrics) showed MIP-Man@EP-treated microbiota closely resembled healthy controls (Figure 6b,c; Figure S25b), indicating a near-complete recovery of the gut microbial community. Mannose intervention groups (Man, NIP-Man@EP) exhibited microbiota shifts diverging from other controls, suggesting mannose modulates microbial composition [19]. Heatmap analysis (Figure 6d) at the genus level revealed MIP-Man@EP group exhibited microbiota characteristics that more closely resembled normal group, whereas Man group demonstrated significant compositional divergence. Critically, compared with the PBS group, MIP-Man@EP treatment significantly reduced *Escherichia-Shigella* [54] (a 36-fold reduction, Enterobacteriaceae, Figure 6e; Figure S26)—pathobionts enriched in human IBD—while increasing probiotic *Lactobacillus* (a 1.4-fold increase, Lactobacillaceae, mucus-promoting) [55] and anti-inflammatory Muribaculaceae (a 3-fold increase, Figure 6f,g) [56]. Concurrent enrichment of Lachnospiraceae (promoting short-chain fatty acid production) [57] further evidenced ecosystem reprogramming (Figure 6h). These results collectively demonstrate synergistic effects of the barrier formation and mannose release in rectifying inflammation-associated dysbiosis.

Furthermore, the concomitant restoration of microbial ecology (Figure 6), attenuation of pro-inflammatory cytokines (Figure 5j–l), mucosal barrier recovery (Figure 5f–i), and ROS-triggered mannose release & binding activation (Figure 4b–f) collectively support a self-limiting therapeutic cascade. In this paradigm, inflammation-derived reactive species initiate saccharide liberation, which in turn promotes barrier restitution and microbial balance, thereby mitigating inflammatory triggers via negative feedback regulation. As a reference point, 5-aminosalicylic acid (5-ASA) is commonly used as a positive-control therapy in DSS-induced colitis models and serves as an established anti-inflammatory benchmark [58, 59]. In our study, beyond cytokine suppression (Figure 5j–l), MIP-Man@EP also restored mucosal barrier markers and tight-junction proteins (Figure 5f–i) and reshaped the microbiota toward a near-healthy profile (Figure 6), supporting a multi-pronged therapeutic mechanism. We note that comparisons to 5-ASA across studies are qualitative given differences in DSS protocols and dosing; head-to-head evaluation with a 5-ASA arm will be pursued in future work.

3 | Conclusion

This study establishes a transformative paradigm for oral intestinal targeting through the rational design of intelligent synthetic antibody mimetics. The core of our design lies in employing the therapeutic payload—here, saccharides—to sterically block the binding capacity of molecularly imprinted polymers (MIP). The linker between the MIP and the saccharide is specifically cleaved in the pathological microenvironment. This triggers the release of the saccharide for therapeutic action while simultaneously restoring the MIP's targeting ability—enabling it to anchor to the inflamed epithelium and form protective barriers. This strategy elegantly resolves the long-standing challenges of in vivo targeting posed by the instability of biological recognition elements and the "always-on" binding state of conventional MIP. Moreover, this work represents the first successful implementation of targeted saccharide intervention in the colon, overcoming the inefficiencies and systemic side effects associated with traditional high-dose oral administration.

In murine colitis models, MIP-Man@EP demonstrated high targeting specificity (22.4-fold enrichment) and sustained retention at the disease site (Figure 4). The exceptional performance can be attributed to the multivalent binding of MIP, its resistance to enzymatic degradation, and the effective prevention of nonspecific adsorption during transit. Furthermore, upon sensing the elevated ROS levels characteristic of inflammation, MIP-Man@EP initiates a cascade of actions. This cascade collectively addresses the multifactorial pathology of IBD—including promotion of barrier repair, mitigation of inflammation, and

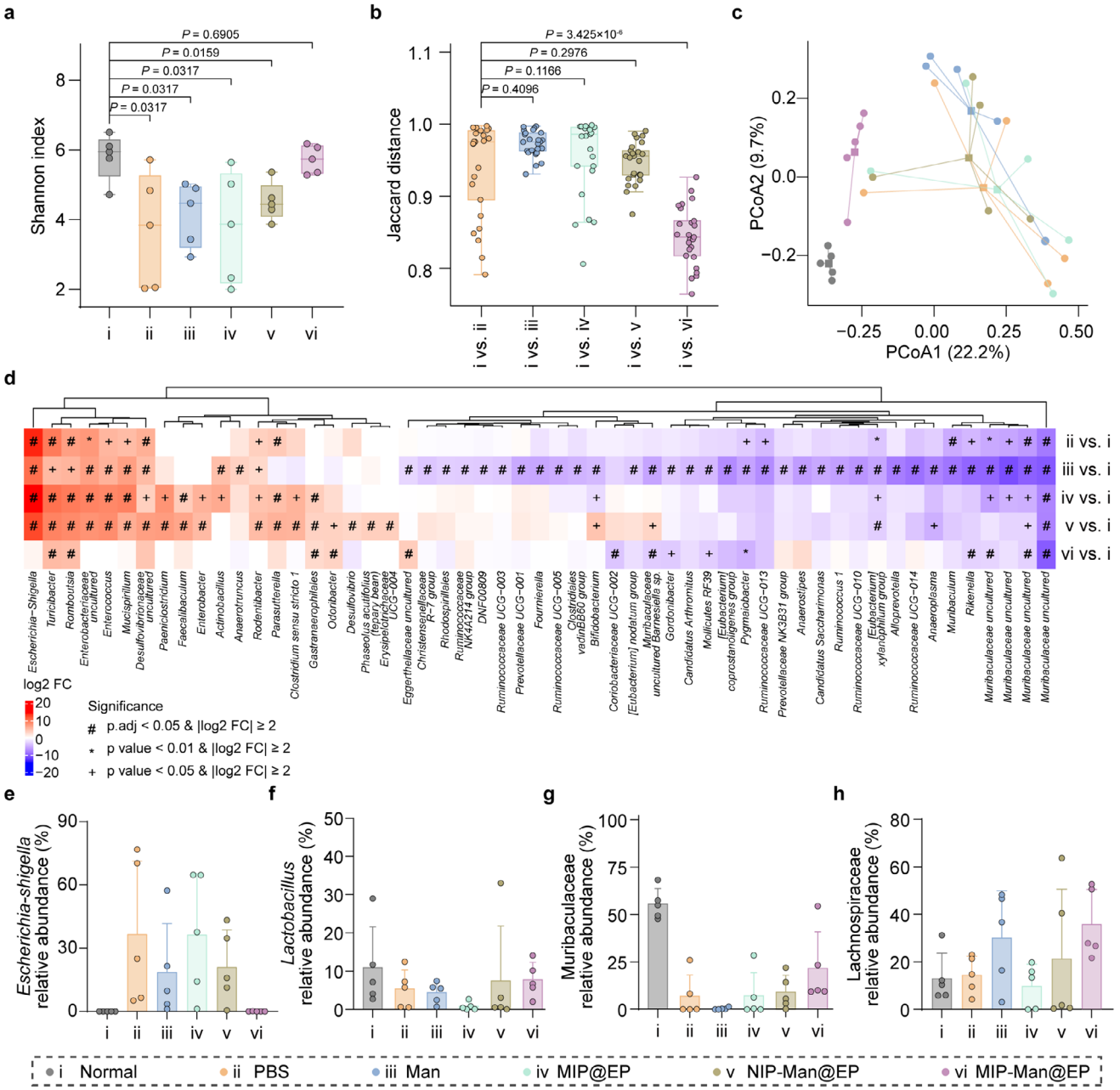

FIGURE 6 | Gut microbiota modulation by MIP-Man@EP in colitic mice. Fecal samples were collected at day 11 for 16S rRNA sequencing-based microbiota composition analysis. (a) α-Diversity analysis: Shannon index. (b,c) β-Diversity analysis: Each box plot indicates jaccard distance between each treatment group and the normal group (b) and PCoA analysis of jaccard distance between groups, a midpoint connection (indicated by squares) was added between the result points (c). (d) Based on genus-level taxonomic differential analysis, abundance changes of microbial genera in treated groups relative to the normal group are displayed using a dual-color coding system: red denotes statistically significant increases in relative abundance, while blue indicates significant decreases. Log2 FC: Log_2 Fold Change. (e) Decreased relative abundance of *Escherichia-Shigella*. (f–h) Increased relative abundance of *Lactobacillus* (f), Muribaculaceae (g), and Lachnospiraceae (h). Data in (a–h) are representative of two independent experiments ($n = 5$ biologically independent animals). Box plot elements: centre line, median; box limits, upper and lower quartiles; whiskers (error bars), the highest and lowest points within 1.5 interquartile range of the upper and lower quartiles. Data in (e–h) are presented as mean ± SD ($n = 5$ biologically independent animals). *p* values of (a,b) were calculated using the Wilcoxon rank-sum test with Benjamini–Hochberg false discovery rate (FDR) correction. For (d), multiple testing correction within comparative groups was performed via the Benjamini–Hochberg method to control FDR.

restoration of microbiota balance. The designed MIP-Man@EP nanoprobe outperforms interventions based on its individual components or mannose therapy alone. Crucially, comparative analysis of single-component interventions vs. untreated controls revealed distinct functional contributions: the MIP module played a more dominant role in restoring barrier integrity (Figure 5f–i; Figure S23), while released mannose exerted a stronger effect on attenuating inflammation (Figure 5j–l). In terms of microbiota modulation, although oral mannose alone significantly reshaped microbiota composition, only MIP-

Man@EP fully restored near-normal community equilibrium (Figure 6). This finding underscores the necessity for combinatorial modulation strategies targeting IBD's complex pathology. Central to this platform is a self-regulating cycle: inflammation-derived reactive species initiate saccharide liberation, which promotes barrier restitution and microbial balance. This, in turn, mitigates inflammatory triggers via a negative feedback loop.

However, the current study still has areas that warrant further improvement. Because transferrin is abundant in serum, a theoretical off-target risk exists if a fraction of de-gated MIPs reaches systemic circulation and binds soluble transferrin. We expect this risk to be limited because oral systemic exposure to intact nanoparticles is generally constrained by intestinal barriers and most material is cleared through the gastrointestinal tract. In addition, circulating particles are likely to adsorb plasma proteins (protein corona) that can occupy cavity entrances and reduce binding competence; consistent with this notion, even limited non-target pre-adsorption markedly suppressed subsequent transferrin binding in our selectivity assays (Figure S2). Nevertheless, quantitative evaluation of systemic exposure, biodistribution/excretion, plasma transferrin binding, and immunogenicity will be essential for translation, as also emphasized in recent IBD biomarker-responsive nanomaterial reviews [60].

While the H_2O_2-triggered recovery of transferrin binding (Figure 3f) confirms the operational success of our gating mechanism, the incomplete restoration (approximately 65%) highlights an area for improvement, especially under the complexity of in vivo conditions. Future iterations of this platform will focus on optimizing the linker chemistry and the design of the protective cloak to achieve more rapid and quantitative release. An additional methodological consideration is the pH-sensitive nature of the FITC label used for imaging; employing pH-insensitive probes in future work will allow for more quantitative biodistribution studies. In addition, these findings were primarily established in preclinical murine models. Future research should rigorously evaluate translational potential in models that better recapitulate human intestinal physiology, with particular attention to long-term safety upon repeated dosing.

This work also opens several promising avenues. Most notably, the platform is inherently generalizable and programmable. By simply altering the imprinting template and payload, the system can be adapted for a wide range of diseases beyond IBD, including cancers, autoimmune disorders, and metabolic syndromes, where precise, context-dependent intervention is needed. It offers a generalizable platform for developing next-generation nanotherapeutics capable of operating with biological precision through purely synthetic means. In addition, the demonstrated capability for in vivo imaging and lesion-specific accumulation suggests potential for theragnostic applications, particularly in guiding endoscopic interventions or monitoring therapeutic responses. Future efforts will focus on advancing the platform toward clinical translation through validation in human-relevant disease models, scaling under GMP conditions, and exploring its utility for delivering diverse therapeutics. By bridging synthetic chemistry, biomaterials science, and targeted therapy, this study not only offers a potent strategy for managing IBD but also provides a foundational framework for the future of intelligent, responsive nanomedicine.

4 | Experimental Section/Methods

4.1 | Materials

D-galactose (Gal), D-lactose (Lac), mannan from Saccharomyces cerevisiae (Mann), *N*,*N*-dimethylformamide (DMF), bovine serum albumin (BSA), and paraffin were obtained from Sigma–Aldrich (USA). D-glucose (Glu) was purchased from Rhawn Reagent (China). D-mannose (Man) and *N*,*N*'-methylenebisacrylamide (MBA) were purchased from Heowns Biochem Technologies. LLc. Tianjin (China). 4-(Hydroxymethyl)phenylboronic acid pinacol ester (HPBAP), 4-carboxyphenylboronic acid (4-CPBA), 2-aminoethyl methacrylate hydrochloride (2-AM) and 1-phenyl-3-methyl-5-pyrazolone (PMP) were obtained from Bide Pharmatech Co., Ltd. (China). Phosphate buffered saline (PBS, containing 136.7 mM NaCl, 2.7 mM KCl, 8.72 mM Na_2HPO_4, 1.41 mM KH_2PO_4) was obtained from Nanjing BioChannel Biotechnology Co., Ltd. (China). Na_2SO_4, petroleum ether (PE), ethyl acetate (EA), silica, MeOH and dichloromethane were purchased from Greagent (China). H_2O_2 was purchased from Alfa Aesar (USA). Ethyl ether, ethanol absolute, HCl (~35%) and $CHCl_3$ were purchased from Nanjing Chemical Reagent Co., Ltd. (China). Fluorescein isothiocyanate (FITC), transferrin (Tf), simulated gastric fluid (SGF), simulated intestinal fluid (SIF), and simulated colonic fluid (SCF) were purchased from Shanghai yuanye Bio-Technology Co., Ltd. (China). IR783 was purchased from TCI Shanghai (China). 3-Aminopropyltriethoxysilane (APTES), tetraethyl orthosilicate (TEOS), *N*,*N*,*N*',*N*'-tetramethylethylenediamine (TEMED), acetic acid, triethylamine and mucin 2 (MUC2) were obtained from Shanghai Macklin Biochemical Co., Ltd. (China). $NH_3 \cdot H_2O$, albumin from chicken egg white, 1-ethyl-(3-dimethylaminopropyl)carbodiimide (EDC), and *N*-hydroxysuccinimide (NHS) were purchased from Shanghai Aladdin Biochemical Technology Co., Ltd. (China). Potassium persulfate (KPS) was purchased from Xilong Scientific Co., Ltd. (China). 4-Nitrophenyl chloroformate and tetrahydrofuran (THF) were purchased from Energy Chemical (China). NaCl, NaOH and acetone were purchased from Sinopharm Chemical Reagent Co., Ltd. (China). $CDCl_3$ was purchased from Adamas (China). D_2O and trifluoroacetic acid (TFA) were purchased from Meryer (Shanghai) Biochemical Technology Co., Ltd. (China). Eudragit S100 (ES100) was purchased from Shanghai Chineway Pharma Tech Co., Ltd. (China). Poly(lactic-co-glycolic acid) (PLGA) was purchased from Xi'an ruixi Biological Technology Co., Ltd. (China). BCA Protein Assay Kit was purchased from Jiangsu CoWin Biotech Co., Ltd. (China). Isoflurane was purchased from RWD Life Science (China). DSS (36000-50000) was purchased from MP Biomedicals (USA). Paraformaldehyde was purchased from Beijing Innochem Science & Technology Co.,Ltd. (China). TRIzol reagent was purchased from Thermo Fisher Scientific (USA). DAPI staining solution, human IL-2 and TNF-α ELISA Kit, and all serum biochemical assay kits were purchased from Beyotime Biotechnology. Aldehyde-

functionalized glass slides were obtained from Shanghai BaiO Technology Co., Ltd. (China). Formvar/Carbon supported copper grids were obtained from Beijing Zhongjingkeyi Technology Co., Ltd. (China). All aqueous solutions were prepared with ultrapure water (≥18 MΩ, Milli-Q, Millipore).

4.2 | Apparatus

The ^{1}H NMR spectra were obtained on the BRUKER AVANCE III 400 MHz system (Bruck, Germany) and the data were analyzed with MestReNova (version 14. 2. 1). The transmission electron microscope (TEM) was performed on JEM-2800 transmission electron microscope (JEOL Ltd., Japan). BCA measurements were performed on a Varioskan Flash Spectral Scanning Multimode Reader (Thermo Fisher Scientific, USA) and the data was processed in Microsoft Excel software 2019. Fluorescent slides were imaged on the ChemiDoc XRS+ Gel Imaging System (Bio-Rad, USA). The animal imaging was performed on IVIS Lumina XRMS III in vivo imaging system (PerkinElmer, USA) and NIR-II fluorescence in vivo imaging system (NIROPTICS, China). Fluorescence labeled colonic sections were imaged on SP8 stimulated emission depletion (STED) 3X confocal laser scanning microscopy (CLSM, Leica, Germany) and the images were analyzed with Leica Application Suite X (LAS X, version 3.3.0). The flow cytometric analysis was carried out on the CytoFLEX (Beckman, USA). HE stained tissue sections were imaged on a Zeiss LSM 880 Confocal Laser Scanning Microscope (Carl Zeiss, Germany). Zeta potential analysis was performed on Zetasizer Nano Z (Malvern Panalytical, UK). Prominence LC-20A high performance liquid chromatography (HPLC, SHIMADZU, Japan) was used for quantification of saccharides. The colon segments were homogenized using a Gastprp-64 high throughput tissue grinder (SHANGHAI JINGXIN, China).

4.3 | Preparation of MIP Carrier

We use fluorescence (FITC or IR783)-doped, carboxyphenylboronic acid (CPBA)-functionalized SiO_2 nanoparticles as the MIP carrier. Fluorescent SiO_2 nanoparticles were first prepared using a modified literature method: [61] A precursor solution containing 2 mg FITC or IR783 and 10 μL (3-aminopropyl)triethoxysilane (APTES) in 1 mL ethanol was incubated at room temperature for 4 h in the dark. Subsequently, 2.425 mL water and 1.8 mL ammonia were added to 20 mL anhydrous ethanol containing the precursor solution. After stirring at 50°C for 10 min, 500 μL tetraethyl orthosilicate (TEOS) was added to initiate 50 min of reaction under stirring. This was followed by adding 3 mL APTES and continuing stirring at 25°C for 24 h to obtain fluorescence-doped, amine-functionalized SiO_2 nanoparticles (SiO_2–NH_2). The product was collected via centrifugation at 10 000 rpm for 5 min with three ethanol washes.

For CPBA functionalization, 120 mg CPBA was activated with 120 mg N-hydroxysuccinimide (NHS) and 240 mg 1-ethyl-3-(3-dimethylaminopropyl) carbodiimide (EDC) in 10 mL dimethylformamide (DMF) at room temperature for 20 min. After adding 100 mg SiO_2-NH_2, the reaction proceeded at 25°C for 12 h under stirring. The final CPBA-functionalized nanoparticles (SiO_2-CPBA) were isolated by centrifugation at 10 000 rpm for 5 min and washed three times with ethanol.

4.4 | Preparation of MIP

The SiO_2-CPBA nanoparticles (1 mg) were incubated with 1 mL of 400 μg mL^{-1} transferrin (Tf) solution at 25°C for 2 h under shaking to form SiO_2-Tf nanoparticles. After centrifugation at 10 000 rpm for 3 min and two PBS (pH 7.4) washes, the nanoparticles were collected for subsequent steps.

The pre-assembly solution was prepared by dispersing 22 mg 2-aminoethyl methacrylate hydrochloride (2-AM) and 20 mg SiO_2-Tf nanoparticles in 1 mL PBS, followed by 6 h incubation at 37°C under shaking. The polymerization system contained 3.7 mg *N*,*N*'-methylenebisacrylamide (crosslinker), 1 mg potassium persulfate (KPS, initiator), and 1 μL *N*,*N*,*N*',*N*'-tetramethylethylenediamine (TEMED, catalyst). The mixture was transferred to a Schlenk tube, sealed, frozen in liquid nitrogen, and deoxygenated under nitrogen for 15 min. Polymerization was conducted at 37°C for 12 h with stirring.

The reaction was terminated by air exposure, with nanoparticles collected via centrifugation (10 000 rpm, 3 min) and washed three times with PBS to eliminate unreacted components. Template removal involved treating 10 mg nanoparticles with 1 mL 0.1 M acetic acid under shaking at 25°C for 2 h, repeated until Tf became undetectable in the supernatant. The as-prepared nanoparticles are named as MIP. Non-imprinted polymer (NIP) was synthesized identically, except omitting Tf during the imprinting step.

4.5 | Saccharide Conjugation and Release Studies

The 4-(hydroxymethyl)phenylboronic acid-saccharide complexes were synthesized through the following procedure: A solution containing 0.3 mmol of monosaccharide (glucose (Glc), mannose (Man), galactose (Gal)) or disaccharide (lactose (Lac)), or 70 mg of mannan (Mann), was combined with 3 mmol of 4-(hydroxymethyl)phenylboronic acid pinacol ester (HPBAP) in 5 mL PBS (pH 7.4). The reaction mixture was stirred at room temperature for 12 h, followed by multiple washes with CH_2Cl_2 to remove unreacted boronic ester. The aqueous phase was lyophilized to yield the HPBAP-saccharide complex as a white solid. Structural verification was performed by ^{1}H NMR analysis.

For saccharide release studies, 20 mg of the synthesized complex was treated with 1 mL of 20 mM H_2O_2 aqueous solution at 25°C for 12 h. After reaction completion, the mixture underwent multiple diethyl ether washes to eliminate hydrophobic byproducts. The remaining aqueous phase was lyophilized and analyzed by ^{1}H NMR. All chemical shifts are reported in ppm relative to tetramethylsilane.

4.6 | Synthesis of 4-Nitrophenyl 4-(4,4,5,5-Tetramethyl-1,3,2-Dioxaborolan-2-yl)Benzyl Carbonate (NBC)

The boronate-functionalized linker NBC was synthesized via a literature method: [38] 5.0 mmol of 4-(hydroxymethyl)phenylboronic acid pinacol ester and 5.6 mmol of 4-nitrophenyl chloroformate were dissolved in 15 mL tetrahydrofuran (THF). Triethylamine (TEA, 10.0 mmol)

was added dropwise to the solution maintained at 0°C. The reaction was stirred at room temperature for 6 h, followed by rotary evaporation to remove solvent. The residue was diluted with dichloromethane (DCM) and sequentially washed with deionized water and saturated NaCl solution. The organic phase was dried over anhydrous sodium sulfate, concentrated by rotary evaporation to obtain the crude product. Purification was performed using silica gel column chromatography with petroleum ether/ethyl acetate (10:1, v/v) as eluent, yielding NBC as a white powder. Structural confirmation was achieved through ^{1}H NMR analysis, with chemical shifts referenced in ppm relative to tetramethylsilane.

4.7 | Preparation of MIP-Saccharide Nanoparticles

The MIP nanoparticles (10 mg) were dispersed in 1 mL DMF containing 6 mg NBC. Triethylamine (4.5 μL) was added dropwise to the mixture under stirring at 25°C. The reaction was allowed to proceed for a further 12 h, after which the nanoparticles were collected via centrifugation (10 000 rpm, 3 min) and washed three times with PBS.

For saccharide conjugation, 10 mg of the nanoparticles were incubated with 1 mL of 2 mg mL^{-1} saccharide solution (Glc, Man, Gal, Lac, or Mann) at 25°C for 12 h under stirring. The MIP-saccharide nanoparticles were collected by centrifugation at 10 000 rpm for 3 min and washed three times with PBS.

4.8 | Fabrication of MIP-Man@EP Nanoparticles

MIP-Man nanoparticles (10 mg) were suspended in 5 mL PBS (pH 5.0). An acetone solution (1 mL) containing 1 mg ES100 and 1 mg PLGA was introduced dropwise into the suspension under continuous stirring. Following 1 h reaction at room temperature, the MIP-Man@EP nanoparticles were harvested via centrifugation (10 000 rpm, 3 min) and subjected to three washing cycles with pH 5.0 PBS.

4.9 | Transmission Electron Microscope (TEM)

Nanoparticle suspensions were diluted to 10 mg mL^{-1}, and 100 μL aliquots were deposited on Formvar/Carbon-coated 200-mesh copper grids and dried at 60°C for measurement.

4.10 | Zeta Potential Analysis

Dispersions (20 mg mL^{-1}) were analyzed at 25°C using a Zetasizer Nano ZS instrument.

4.11 | Binding Isotherm Analysis for MIP

MIP or NIP nanoparticles (1 mg) were equilibrated with 1 mL transferrin (Tf) solutions (0.025–0.8 mg mL^{-1} in PBS, pH 7.4) at 37°C for 2 h under shaking. Following incubation, the supernatant was collected via centrifugation, and Tf concentration (i.e., equilibrium concentration, C_e, μg·mL^{-1}) was quantified using a BCA protein assay. Tf concentration in the nanoparticle-free protein control was also measured as C_0 (initial concentration, μg·mL^{-1}). The binding capacity (Q, μg Tf per mg nanoparticles, μg·mg^{-1}) was calculated using:

$$Q = (C_0 - C_e) \times V / W \quad (1)$$

where V = solution volume (mL), and W = nanoparticle mass (mg).

4.12 | Protein Selectivity Assessment for MIP

The protein binding selectivity of MIP was evaluated using two independent assay systems: To detect the binding ability of MIP and NIP toward target proteins in solution, MIP or NIP nanoparticles (1 mg) were incubated with 1 mL solutions of transferrin (Tf), bovine serum albumin (BSA), mucin 2 (MUC2), or albumin (ALB) (1 mg mL^{-1} each in PBS, pH 7.4). After continuous shaking at 37°C for 2 h, supernatants were collected by centrifugation. Residual protein concentrations (C_e) were quantified using a BCA assay. Protein concentration in each nanoparticle-free protein control was also measured as C_0. The binding capacity (Q, μg·mg^{-1}) of MIP (Q_{MIP}) and NIP (Q_{NIP}) was calculated according to Equation (1). And the selectivity was evaluated by the imprinting factor (*IF*):

$$IF = Q_{MIP} / Q_{NIP} \quad (2)$$

To detect the binding ability of MIP and NIP toward target proteins anchored on substrates, aldehyde-functionalized glass slides were sectioned into discrete 8-mm diameter reaction chambers using porous stickers. Each chamber received 8 μL of protein solution (30 mg mL^{-1} in PBS): transferrin, MUC2, or BSA. After 12 h incubation at 37°C, chambers were rinsed with PBS. MIP/NIP nanoparticles (8 μL, 10 mg mL^{-1}) were delivered to corresponding chambers and incubated at 37°C for 2 h in a light-tight humidified chamber. Unbound nanoparticles were removed by PBS washing. Bound particles were imaged using a Bio-Rad ChemiDoc XRS+ system.

4.13 | Evaluation of Transferrin-Binding Capacity of MIP After Nonspecific Protein Adsorption

MIP (1 mg) were first incubated with 1 mL solutions of bovine serum albumin (BSA), mucin 2 (MUC2), or albumin (ALB) (1 mg mL^{-1} each in PBS, pH 7.4) under continuous shaking at 37°C for 2 h. After centrifugation, the supernatants were discarded, and the particles were then subjected to incubation with transferrin solution (0.5 mg mL^{-1}, 1 mL) for 2 h at 37°C. Finally, the supernatants were collected by centrifugation, and the transferrin binding capacity (Q, μg·mg^{-1}) was calculated according to Equation (1).

4.14 | H_2O_2-Responsive Saccharide Release from MIP

MIP-saccharide nanoparticles (10 mg; types: Glc, Gal, Man, Lac, Mann) were dispersed in 1 mL of 0.5 mM H_2O_2, and the mixture was stirred at 37°C for 4 h. The supernatant was then collected by centrifugation (10 000 rpm, 3 min) and lyophilized to isolate released saccharides.

4.15 | Saccharide-Regulated Transferrin Recognition Analysis

To evaluate the impact of saccharide conjugation/release on MIP recognition, two sample sets were prepared:

(1) Saccharide-conjugated MIP: MIP-Man and MIP-Mann nanoparticles.
(2) H_2O_2-treated MIP-Man and MIP-Mann: MIP-Man or MIP-Mann nanoparticles (10 mg) were dispersed in 1 mL of 0.5 mM H_2O_2, stirred at 37°C for 4 h, collected by centrifugation (10 000 rpm, 3 min), and washed thrice with PBS.

Nanoparticles (10 mg) were incubated with 1 mL transferrin solution (0.5 mg mL^{-1}) at 37°C for 2 h with shaking. Supernatants were collected by centrifugation. Transferrin concentration in supernatant (C_e) was determined using a BCA Protein Assay Kit. Transferrin concentration in the nanoparticle-free protein control was also measured as C_0. Transferrin binding capacity (Q, μg·mg^{-1}) was calculated according to Equation (1).

4.16 | Saccharide Release Kinetics of MIP-Man@EP Under Different Physiological Conditions

MIP-Man@EP nanoparticles (10 mg) were incubated under three physiologically relevant conditions:

(1) Simulated gastric fluid: 1 mL PBS, pH 2.0
(2) Simulated colonic fluid: 1 mL PBS, pH 7.4
(3) Simulated inflamed colonic fluid: 1 mL PBS (pH 7.4) containing 180 μM H_2O_2

Following 4 h incubation at 37°C, supernatants were collected by centrifugation (10 000 rpm, 3 min). Mannose concentrations in supernatants were quantified by HPLC.

4.17 | Transferrin Binding Capacity of Processed MIP-Man@EP

Three nanoparticle samples were evaluated:

(1) MIP-Man@EP (10 mg) incubated in 1 mL pH 2.0 PBS (37°C, 4 h)
(2) MIP-Man@EP (10 mg) incubated in 1 mL pH 7.4 PBS (37°C, 4 h)
(3) MIP-Man@EP (10 mg) incubated in 1 mL pH 7.4 PBS with 180 μM H_2O_2 (37°C, 4 h)

Following treatment, nanoparticles were harvested by centrifugation, rinsed, and incubated with 1 mL transferrin solution (0.5 mg mL^{-1}). After 2 h shaking at 37°C, supernatants were collected by centrifugation. Transferrin binding capacity (Q, μg·mg^{-1}) was calculated following established methods.

4.18 | Transferrin Binding Capacity of MIP-Man@EP and MIP@EP During Simulated Delivery

To evaluate the nonspecific adsorption: MIP-Man@EP or MIP@EP nanoparticles (10 mg) were respectively subjected to two different procedures:

(1) Incubation in 1 mL of simulated gastric fluid (SGF, 37°C, 4 h);
(2) Sequential incubation in 1 mL of SGF (37°C, 4 h) and simulated intestinal fluid (SIF, 37°C, 2 h).

After final incubation, the supernatant was collected via centrifugation, and the protein concentration in the simulated fluids (i.e., equilibrium concentration, C_{en}, μg·mL^{-1}) was quantified using a BCA protein assay. The protein concentration in the control fluids without nanoparticle added was also measured as C_{0n} (initial concentration, μg·mL^{-1}). The binding capacity (Q_n, μg protein per mg nanoparticles, μg·mg^{-1}) was calculated using:

$$Q_n = (C_{0n} - C_{en}) \times V / W \quad (3)$$

where V = solution volume (mL), and W = nanoparticle mass (mg).

To evaluate Tf adsorption capability: MIP-Man@EP or MIP@EP nanoparticles (10 mg) were respectively subjected to three different treatment procedures:

(1) Sequential incubation in 1 mL of SGF (37°C, 4 h) and PBS (pH 7.4, containing 0.5 mg mL^{-1} transferrin and 180 μM H_2O_2, 37°C, 2 h);
(2) Sequential incubation in 1 mL of SGF (37°C, 4 h), SIF (37°C, 2 h), and finally PBS (pH 7.4, containing 0.5 mg mL^{-1} transferrin and 180 μM H_2O_2, 37°C, 2 h);
(3) Sequential incubation in 1 mL of SGF (37°C, 4 h), SIF (37°C, 2 h), and finally simulated colonic fluid (SCF, containing 0.5 mg mL^{-1} transferrin and 180 μM H_2O_2, 37°C, 4 h).

The transferrin binding capacity (Q, μg·mg^{-1}) was calculated according to Equation (1).

4.19 | HPLC Saccharide Quantification

For analysis of Man, Glc, Gal, or Lac after H_2O_2 treatment, supernatants were centrifuged and lyophilized. The powder was dissolved in 400 μL H_2O, mixed with 400 μL 0.3 M NaOH and 400 μL 0.5 M 1-phenyl-3-methyl-5-pyrazolone (PMP) in methanol, heated (70°C, 90 min), cooled, neutralized with 500 μL 0.3 M HCl, and extracted thrice with chloroform (2 mL per extraction). Derivatives in aqueous solution were analyzed by HPLC.

For analysis of mannan after H_2O_2 treatment, the lyophilized powder was dissolved in 500 μL 4 M TFA, hydrolyzed (80°C, 5 h), and TFA evaporated. The residue was dissolved in 400 μL H_2O, then derivatized identically as described above.

The conditions of HPLC parameters as follow: Column: Thermo Fisher C18 (4.6 × 50 mm), particle size 1.8 μm, at room temperature. Detection wavelength: 250 nm. Mobile phase A: 70% 0.2 M aqueous ammonium acetate. Mobile phase B: 30% acetonitrile. Injection volume: 20 μL. Flow rate: 0.8 mL min^{-1}. Analysis duration: 15 min per sample.

4.20 | Animals

All animal experimental procedures were conducted in accordance with protocols approved by the Institutional Animal Care and Use Committee (IACUC) of Nanjing University (approval number IACUC-2502008).

4.21 | Induction of Colitis in Mice Using DSS

Female C57BL/6 mice (8 weeks old; GemPharmatech) were group-housed (5 per cage) with a 7-day acclimatization period. Colitis was induced by administering 2.5% (w/v) dextran sulfate sodium (DSS, 36–50 kDa) in drinking water ad libitum for 7 days, followed by normal water. Healthy control mice received normal water throughout.

4.22 | In Vivo Colonic Binding Behavior of MIP

To evaluate targeting specificity, mice (n = 3 per group: normal and DSS-induced colitis) received intrarectal administration of MIP (150 μL, 40 mg mL^{-1} in PBS). Following 4 h post-administration incubation, mice were euthanized. Excised colons were PBS-rinsed and immediately imaged using an IVIS Lumina XRMS III system ($\lambda_{ex}/\lambda_{em}$: 488/493–517 nm). Fluorescence intensity was quantified using Living Image 4.4 software. Parallel experiments with NIP control (150 μL, 40 mg mL^{-1} in PBS) were conducted under identical conditions.

4.23 | Targeting Efficiency Assessment using IR783-Doped Nanoprobes

Normal and DSS-induced colitis mice (n = 3/group) received oral gavage of IR783-doped MIP-Man@EP (MIP-Man@EP (IR783); 80 mg mL^{-1} in PBS, pH 5.0; 200 μL). After 22 h, mice were anesthetized (isoflurane) and subjected to in vivo NIR-II fluorescence imaging. Following euthanasia, excised colons underwent ex vivo NIR-II imaging.

DSS-colitis mice received either IR783-doped MIP-Man@EP or NIP-Man@EP (80 mg mL^{-1} in PBS; n = 1 per group). At 24 h post-administration, in vivo NIR-II imaging was performed under isoflurane anesthesia, followed by ex vivo colon imaging after euthanasia.

Excitation wavelength: 808 nm; laser energy: 10 W; emission was collected with a 900 nm long-pass filter. MFI is calculated by dividing the total fluorescence signal of the colon tissue area by the corresponding area in pixels.

4.24 | Binding Kinetics of MIP-Man@EP (IR783)

Normal and DSS-colitis mice (n = 5/group) received oral gavage of IR783-doped MIP-Man@EP (80 mg mL^{-1} in PBS, pH 5.0; 200 μL). At designated time points (4, 8, 12, 16, or 24 h), one mouse per group was randomly selected for NIR-II imaging and subsequently euthanized. The gastrointestinal tracts were excised and immediately subjected to NIR-II imaging.

4.25 | Targeting Validation using FITC-Doped MIP-Man@EP

Normal and DSS-colitis mice (n = 5/group) received oral gavage of FITC-doped MIP-Man@EP (80 mg mL^{-1} in PBS, pH 5.0; 200 μL). After 24 h, colons were excised and imaged using an IVIS Lumina XRMS III system ($\lambda_{ex}/\lambda_{em}$: 488/493–517 nm). Fluorescence intensity was quantified (Living Image v4.4).

Colon sections were DAPI-counter-stained and imaged by an SP8 STED 3X confocal microscope with the following settings: DAPI, 405 nm excitation/420–500 nm emission; FITC, 488 nm excitation/500–550 nm emission.

4.26 | Therapeutic Evaluation of MIP-Man@EP in Murine Colitis Model

Mice were randomly allocated to six groups (n = 5):

1. Normal control: Standard drinking water without interventions.
2. (2–6) Treatment groups: Received 2.5% (w/v) DSS in drinking water for 6 days. From Day 3 to Day 10 the following solutions (1 administrations/day) were administered via daily oral gavages:
3. (2) PBS control: PBS (pH 5.0, 200 μL)
4. (3) Man: 2.56 mg mL^{-1} mannose in PBS (pH 5.0, 200 μL)
5. (4) MIP@EP: 80 mg mL^{-1} MIP@EP in PBS (pH 5.0, 200 μL)
6. (5) NIP-Man@EP: 80 mg mL^{-1} NIP-Man@EP in PBS (pH 5.0, 200 μL)
7. (6) MIP-Man@EP: 80 mg mL^{-1} MIP-Man@EP in PBS (pH 5.0, 200 μL)

Body weight was recorded daily. At endpoint, disease activity index (DAI) was evaluated, fecal samples collected for microbiome analysis, and mice euthanized. Colon length was measured immediately post-euthanasia. After gentle PBS perfusion, a 0.5 cm distal colon segment underwent histological assessment and immunofluorescence. Remaining tissue was analyzed for inflammatory cytokines.

DAI scoring criteria:

Percentage of body weight loss: no loss = 0, 1%–5% = 1, 5%–10% = 2, 10%–15% = 3, >15% = 4;

Fecal consistency: hard = 0, soft = 2, runny = 4;

Fecal bleeding: no blood = 0, presence of blood = 2, visible bleeding = 4.

The DAI score was obtained by dividing the total score by three.

4.27 | Histopathological Evaluation

Distal colon segments were fixed in 4% paraformaldehyde (8 h), dehydrated through ethanol gradients, paraffin-embedded, sectioned (5 μm), and H&E-stained. The colonic histological damage was evaluated using a blinded approach according to the scoring system [62].

Colonic damage scores were as follows: normal = 0; hyperproliferation, irregular crypts and loss of goblet cell = 1; Mild to moderate crypt loss (10%–50%) = 2; Serious crypt loss (50%–90%) = 3; complete crypts loss, surface epithelium intact = 4; small- to medium-sized ulcers (<10 crypt widths) = 5; large ulcers (≥10 crypt widths) = 6.

Inflammatory cell infiltration was scored based on the mucosa (normal = 0; mild = 1; modest = 2; severe = 3), submucosa (normal = 0; mild to modest = 1; severe = 2) and muscle/serosa (normal = 0; moderate to severe = 1).

These scores are added together to give a total score ranging from 0 to 12.

4.28 | Immunofluorescence Imaging

Tissue sections underwent antigen retrieval by heating at 100°C for 15 min. After blocking with goat serum (1 h, room temperature), slides were incubated with primary antibodies at 4°C overnight: rabbit anti-ZO-1 (1:200, Aifang Biological), rabbit anti-occludin (1:200, Proteintech), and rabbit anti-MUC2 (1:1000, Abcam). Secondary antibody incubation was performed for 1 h at room temperature using Alexa Fluor 488-conjugated antibody (Anti-rabbit IgG (H+L), Invitrogen) for MUC2 and Alexa Fluor 546-conjugated antibodies (Anti-rabbit IgG (H+L), Invitrogen) for ZO-1 and occludin. Nuclei were counter-stained with DAPI. Imaging was performed using an SP8 STED 3X confocal microscope with the following settings: 488 nm excitation/500–550 nm emission or 546 nm excitation/560–610 nm emission.

4.29 | Reverse Transcription Quantitative PCR (RT-qPCR)

Total RNA was extracted from colon tissues using TRIzol reagent. Following manufacturer instructions, 1 μg RNA was reverse transcribed with HiScript III RT SuperMix for qRT-PCR (+gDNA wiper). cDNA was amplified using ChamQ SYBR qPCR Master Mix (High ROX Premixed) on an Applied Biosystems StepOnePlusTM system. Relative gene expression was calculated via the 2−ΔΔCT method.

The following primer sequences were used for amplification:

mTNF-α

FW: 5'-GTGCACGGTCACCTATGAGAATG-3';

RV: 5'-GGCTTCGTTCTGTCCCACTG-3'

mIL-1β

FW: 5'-TCCTTCATCTTTGAAGAAGAGCCC-3';

RV: 5'-ATGGGAACGTCACACACCAG-3'

mIL-6

FW: 5'-CTGGTCTTCTGGAGTACCATAGC-3';

RV: 5'-CTGAAGGACTCTGGCTTTGTC-3'

mGAPDH

FW: 5'-GAAGGGCTCATGACCACAG-3';

RV: 5'-AGATCCACGACGGACACATT-3'

4.30 | In Vitro Anti-inflammatory Effect Invaluation

The anti-inflammatory effect of mannose was assessed using a cellular model of intestinal inflammation. Caco2 cells were purchased from ATCC (American Type Culture Collection). Caco2 cells were cultured in DMEM supplemented with 10% fetal bovine serum (FBS). To establish an inflammatory model, cells were stimulated for 24 h with 1 μg mL-1 lipopolysaccharide (LPS) [63]. After LPS stimulation, cells were treated for 12 h with one of the following: 1 mL of 10 mg mL^{-1} MIP, 0.34 mg mL^{-1} free mannose (an equivalent dose to the payload carried by 10 mg of MIP-Man), or a physical mixture of MIP and free mannose at the aforementioned concentrations. After incubation, cell culture supernatants were collected, lyophilized, and reconstituted in 100 μL PBS. The concentrations of the pro-inflammatory cytokines interleukin-2 (IL-2) and tumor necrosis factor-alpha (TNF-α) were quantified using specific enzyme-linked immunosorbent assay (ELISA) kits according to the manufacturers' protocols.

4.31 | Gut Microbiome Analysis

Total genomic DNA was extracted via the CTAB method. DNA concentration and purity were assessed by 1% agarose gel electrophoresis. Samples were diluted to 1 ng·μL-1 in nuclease-free water. The V3-V4 region of bacterial 16S rRNA genes was amplified using barcoded primers 341F (5'-CCTAYGGGRBGCASCAG-3') and 806R (5'-GGACTACNNGGGTATCTAAT-3'). All PCR reactions were carried out with 15 μL of Phusion High-Fidelity

PCR Master Mix (New England Biolabs, USA); 2 μM of forward and reverse primers, and about 10 ng template DNA. Thermal cycling consisted of initial denaturation at 98°C for 1 min, followed by 30 cycles of denaturation at 98°C for 10 s, annealing at 50°C for 30 s, and elongation at 72°C for 30 s. Finally, 72°C for 5 min.

Amplified products were mixed 1:1 with loading buffer (1×, SYBR Green-containing), visualized on 2% agarose gels, pooled equimolarly, and purified (Qiagen Gel Extraction Kit). Sequencing libraries were prepared with the TruSeq DNA PCR-Free Kit (Illumina), with the addition of index codes. Library quality was verified using Qubit 2.0 (Thermo Scientific) and Bioanalyzer 2100 (Agilent). Paired-end sequencing (250 bp) was performed on Illumina NovaSeq.

Sequences were analyzed using QIIME 2 software and phylogenetic tree was constructed using the 'align-to-tree-mafft-fasttree' q2-phylogeny plugin with the default parameters. Jaccard dissimilarity and unweighted Unifrac distance beta diversity were used to characterize beta diversity, and Shannon index and Faith's phylogenetic diversity were performed to calculate alpha diversity. Pairwise comparisons of genus-level taxonomic composition were performed using Linear discriminant analysis (LinDA) with effect size thresholding.

4.32 | Assessment of Systemic Biosafety and Immunogenicity

To evaluate the systemic safety and immunogenic potential of the MIP-Man@EP, healthy mice were randomly assigned to two groups ($n = 3$ per group): PBS control group and MIP-Man@EP treatment group. Mice in the control group received daily oral gavage of 200 μL PBS (pH 5.0) for 10 consecutive days. Mice in the treatment group received daily oral gavage of 200 μL MIP-Man@EP (80 mg mL^{-1} in PBS, pH 5.0) for the same period. All animals were euthanized on day 11 for sample collection.

4.32.1 | Serum Biochemistry and Histopathology

Blood was collected via orbital sinus puncture, and serum was separated for biochemical analysis. The levels of alanine aminotransferase (ALT), aspartate aminotransferase (AST), alkaline phosphatase (ALP), albumin (ALB), serum creatinine (CREA-S), and uric acid (UA) were measured using standard clinical assay kits. Major organs (heart, liver, spleen, lung, and kidney) were harvested, fixed in 4% paraformaldehyde, dehydrated through a graded ethanol series, embedded in paraffin, sectioned at 5 μm thickness, and stained with hematoxylin and eosin (H&E) for histopathological examination.

4.32.2 | Immunophenotyping of Splenocytes

Spleen were harvested aseptically. Single-cell suspensions were prepared by mechanical dissociation followed by red blood cell lysis. Splenocytes were stained with fluorescently labeled antibodies against mouse CD45, CD11c, CD11b, and CD3 for 30 min at 4°C in the dark. After washing, the cells were analyzed by flow cytometry to determine the counts of total leukocytes ($CD45^+$), dendritic cells ($CD11c^+$), macrophages ($CD11b^+$), and T cells ($CD3^+$).

4.33 | Statistical Analysis

All experiments were independently repeated in triplicate unless otherwise stated. The results are expressed as means ± S.D. Two-sided Student's t-test, one-way analysis of variance (ANOVA) with Tukey's multiple comparisons, and Wilcoxon rank-sum test with Benjamini–Hochberg false discovery rate (FDR) correction were used for testing differences among groups. No samples were excluded from analysis. A value of $P < 0.05$ was considered statistically significant. For Figure 6D, the Benjamini-Hochberg method was applied with statistical significance defined as BH-adjusted $p < 0.1$ and $|\log2\ FC| \geq 2$. GraphPad Prism (version 9.0.0) software was used for all statistical analyses.

Acknowledgements

We gratefully acknowledge support from the National Natural Science Foundation of China (22574077, 22274073), and the State Key Laboratory of Analytical Chemistry for Life Science (5431ZZXM2504).

Funding

National Natural Science Foundation of China (22574077, 22274073); State Key Laboratory of Analytical Chemistry for Life Science (5431ZZXM2504)

Conflicts of Interest

The authors declare no conflicts of interest.

Data Availability Statement

The data that support the findings of this study are available from the corresponding author upon reasonable request.

References

1. J. T. Chang, "Pathophysiology of Inflammatory Bowel Diseases," *New England Journal of Medicine* 383 (2020): 2652–2664, https://doi.org/10.1056/NEJMra2002697.

2. S. Zhang, R. Langer, and G. Traverso, "Nanoparticulate Drug Delivery Systems Targeting Inflammation for Treatment of Inflammatory Bowel Disease," *Nano Today* 16 (2017): 82–96, https://doi.org/10.1016/j.nantod.2017.08.006.

3. M. F. Neurath, "Current and Emerging Therapeutic Targets for IBD," *Nature Reviews Gastroenterology & Hepatology* 14 (2017): 269–278, https://doi.org/10.1038/nrgastro.2016.208.

4. A. R. Moschen, H. Tilg, and T. Raine, "IL-12, IL-23 and IL-17 in IBD: Immunobiology and Therapeutic Targeting," *Nature Reviews Gastroenterology & Hepatology* 15 (2018): 185–196, https://doi.org/10.1038/s41575-018-0084-8.

5. B. E. Sands, W. J. Sandborn, R. Panaccione, et al., "Ustekinumab as Induction and Maintenance Therapy for Ulcerative Colitis," *New England Journal of Medicine* 381 (2019): 1201–1214, https://doi.org/10.1056/NEJMoa1900750.

6. O. Hartwig, M. A. Shetab Boushehri, K. S. Shalaby, B. Loretz, A. Lamprecht, and C.-M. Lehr, "Drug Delivery to the Inflamed Intestinal Mucosa—Targeting Technologies and Human Cell Culture Models for

Better Therapies of IBD," *Advanced Drug Delivery Reviews* 175 (2021): 113828, https://doi.org/10.1016/j.addr.2021.113828.

7. D.-F. Li, M.-F. Yang, H.-M. Xu, et al., "Nanoparticles for Oral Delivery: Targeted Therapy for Inflammatory Bowel Disease," *Journal of Materials Chemistry B* 10 (2022): 5853–5872, https://doi.org/10.1039/d2tb01190e.

8. L. Chen, X. Wang, W. Lu, X. Wu, and J. Li, "Molecular Imprinting: Perspectives and Applications," *Chemical Society Reviews* 45 (2016): 2137–2211, https://doi.org/10.1039/c6cs00061d.

9. J. J. BelBruno, "Molecularly Imprinted Polymers," *Chemical Reviews* 118 (2018): 94–119, https://doi.org/10.1021/acs.chemrev.8b00171.

10. K. Haupt, P. X. Medina Rangel, and B. T. S. Bui, "Molecularly Imprinted Polymers: Antibody Mimics for Bioimaging and Therapy," *Chemical Reviews* 120 (2020): 9554–9582, https://doi.org/10.1021/acs.chemrev.0c00428.

11. M. Zangiabadi, F. Bahrami, A. Ghosh, et al., "Synthetic Catalysts for Selective Glycan Cleavage From Glycoproteins and Cells," *Journal of the American Chemical Society* 146 (2024): 4346–4350, https://doi.org/10.1021/jacs.3c13700.

12. J. Xu, H. Miao, J. Wang, and G. Pan, "Molecularly Imprinted Synthetic Antibodies: From Chemical Design to Biomedical Applications," *Small* 16 (2020): 1906644, https://doi.org/10.1002/smll.201906644.

13. O. Stojanović, I. Miguel-Aliaga, and M. Trajkovski, "Intestinal Plasticity and Metabolism as Regulators of Organismal Energy Homeostasis," *Nature Metabolism* 4 (2022): 1444–1458, https://doi.org/10.1038/s42255-022-00679-6.

14. F. A. Duca, T. M. Z. Waise, W. T. Peppler, and T. K. T. Lam, "The Metabolic Impact of Small Intestinal Nutrient Sensing," *Nature Communications* 12 (2021): 903, https://doi.org/10.1038/s41467-021-21235-y.

15. Y. Litvak, M. X. Byndloss, and A. J. Bäumler, "Colonocyte Metabolism Shapes the Gut Microbiota," *Science* 362 (2018): aat9076, https://doi.org/10.1126/science.aat9076.

16. M. R. Kudelka, S. R. Stowell, R. D. Cummings, and A. S. Neish, "Intestinal Epithelial Glycosylation in Homeostasis and Gut Microbiota Interactions in IBD," *Nature Reviews Gastroenterology & Hepatology* 17 (2020): 597–617, https://doi.org/10.1038/s41575-020-0331-7.

17. P. S. Gonzalez, J. O'Prey, S. Cardaci, et al., "Mannose Impairs Tumour Growth and Enhances Chemotherapy," *Nature* 563 (2018): 719–723, https://doi.org/10.1038/s41586-018-0729-3.

18. A. Bitto, A. S. Grillo, T. K. Ito, et al., "Acarbose Suppresses Symptoms of Mitochondrial Disease in a Mouse Model of Leigh Syndrome," *Nature Metabolism* 5 (2023): 955–967, https://doi.org/10.1038/s42255-023-00815-w.

19. V. Sharma, J. Smolin, J. Nayak, et al., "Mannose Alters Gut Microbiome, Prevents Diet-Induced Obesity, and Improves Host Metabolism," *Cell Reports* 24 (2018): 3087–3098, https://doi.org/10.1016/j.celrep.2018.08.064.

20. Y. Li, Y. Jiang, L. Zhang, W. Qian, X. Hou, and R. Lin, "Exogenous l -Fucose Protects the Intestinal Mucosal Barrier Depending on Upregulation of FUT2-Mediated Fucosylation of Intestinal Epithelial Cells," *The FASEB Journal* 35 (2021): 21699, https://doi.org/10.1096/fj.202002446RRRR.

21. Y. Yao, G. Kim, S. Shafer, et al., "Mucus Sialylation Determines Intestinal Host-commensal Homeostasis," *Cell* 185 (2022): 1172–1188.e28, https://doi.org/10.1016/j.cell.2022.02.013.

22. O. Pabst, M. W. Hornef, F. G. Schaap, V. Cerovic, T. Clavel, and T. Bruns, "Gut–Liver Axis: Barriers and Functional Circuits," *Nature Reviews Gastroenterology & Hepatology* 20 (2023): 447–461, https://doi.org/10.1038/s41575-023-00771-6.

23. M. A. Febbraio and M. Karin, ""Sweet death": Fructose as a Metabolic Toxin that Targets the Gut-Liver Axis," *Cell Metabolism* 33 (2021): 2316–2328, https://doi.org/10.1016/j.cmet.2021.09.004.

24. Y. Harada, Y. Mizote, T. Suzuki, et al., "Metabolic Clogging of Mannose Triggers dNTP Loss and Genomic Instability in human Cancer Cells," *Elife* 12 (2023): 83870, https://doi.org/10.7554/eLife.83870.

25. J. M. Duran, "D-mannose Transport and Metabolism in Isolated Enterocytes," *Glycobiology* 14 (2004): 495–500, https://doi.org/10.1093/glycob/cwh059.

26. S. Zhang, J. Ermann, M. D. Succi, et al., "An Inflammation-Targeting Hydrogel for Local Drug Delivery in Inflammatory Bowel Disease," *Science Translational Medicine* 7 (2015): 300ra128, https://doi.org/10.1126/scitranslmed.aaa5657.

27. B. Tirosh, N. Khatib, Y. Barenholz, A. Nissan, and A. Rubinstein, "Transferrin as a Luminal Target for Negatively Charged Liposomes in the Inflamed Colonic Mucosa," *Molecular Pharmaceutics* 6 (2009): 1083–1091, https://doi.org/10.1021/mp9000926.

28. Z. Chen, Y.-X. Zhu, Y. You, et al., "Enzyme-mimic Activities of RuCo Bimetallic Nanosheets for Inflammatory Bowel Disease Treatment," *Journal of the American Chemical Society* 147 (2025): 13424–13436, https://doi.org/10.1021/jacs.5c00100.

29. X. Sun, B. M. Chapin, P. Metola, et al., "The Mechanisms of Boronate Ester Formation and Fluorescent Turn-on in Ortho-aminomethylphenylboronic Acids," *Nature Chemistry* 11 (2019): 768–778, https://doi.org/10.1038/s41557-019-0314-x.

30. J. Yu, J. Wang, and Y. Zhang, "Glucose-responsive Insulin Patch for the Regulation of Blood Glucose in Mice and Minipigs," *Nature Biomedical Engineering* 4 (2020): 499–506, https://doi.org/10.1038/s41551-019-0508-y.

31. L. Dong, J. Xie, Y. Wang, et al., "Mannose Ameliorates Experimental Colitis by Protecting Intestinal Barrier Integrity," *Nature Communications* 13 (2022): 4808, https://doi.org/10.1038/s41467-022-32505-8.

32. P. Xiao, Z. Hu, J. Lang, et al., "Mannose Metabolism Normalizes Gut Homeostasis by Blocking the TNF-α-mediated Proinflammatory Circuit," *Cellular & Molecular Immunology* 20 (2023): 119–130, https://doi.org/10.1038/s41423-022-00955-1.

33. C. Huang, J. Xu, J. Li, et al., "Hydrogen Peroxide Responsive Covalent Cyclodextrin Framework for Targeted Therapy of Inflammatory Bowel Disease," *Carbohydrate Polymers* 285 (2022): 119252, https://doi.org/10.1016/j.carbpol.2022.119252.

34. G. Dalmasso, E. Harel, A. Rubinstein, et al., "Enhanced Transferrin Receptor Expression by Proinflammatory Cytokines in Enterocytes as a Means for Local Delivery of Drugs to Inflamed Gut Mucosa," *PLoS ONE* 6 (2011): 24202, https://doi.org/10.1371/journal.pone.0024202.

35. P. Gallego, M. Garcia-Bonete, S. Trillo-Muyo, C. V. Recktenwald, M. E. V. Johansson, and G. C. Hansson, "The Intestinal MUC2 Mucin C-terminus Is Stabilized by an Extra Disulfide Bond in Comparison to von Willebrand Factor and Other Gel-forming Mucins," *Nature Communications* 14 (2023): 1969, https://doi.org/10.1038/s41467-023-37666-8.

36. E. E. L. Nyström, B. Martinez-Abad, L. Arike, et al., "An Intercrypt Subpopulation of Goblet Cells Is Essential for Colonic Mucus Barrier Function," *Science* 372 (2021): abb1590.

37. C. Tacconi, S. Schwager, and N. Cousin, "Antibody-mediated Delivery of VEGFC Ameliorates Experimental Chronic Colitis," *ACS Pharmacology & Translational Science* 2 (2019): 342–352, https://doi.org/10.1021/acsptsci.9b00037.

38. E. Tan, T. Wan, C. Yu, et al., "ROS-responsive Polypeptides for Intracellular Protein Delivery and CRISPR/Cas9 Gene Editing," *Nano Today* 46 (2022): 101617, https://doi.org/10.1016/j.nantod.2022.101617.

39. L. Cheng, Y. Dai, N. Zhang, et al., "Cu–Zn@HA Bimetallic Nanozymes: A Novel Approach for ROS Clearance and Macrophage Polarization in Colitis therapy," *Advanced Composites and Hybrid Materials* 8, (2025): 197.

40. P. S. Haque, N. Kapur, T. A. Barrett, and A. L. Theiss, "Mitochondrial Function and Gastrointestinal Diseases," *Nature Reviews Gastroenterol-*

ogy & Hepatology 21 (2024): 537–555, https://doi.org/10.1038/s41575-024-00931-2.

41. Z. Zeng, J. Ouyang, L. Sun, F. Zeng, and S. Wu, "A Biomarker-Responsive Nanosystem With Colon-Targeted Delivery for Ulcerative Colitis's Detection and Treatment With Optoacoustic/NIR-II Fluorescence Imaging," *Advanced Healthcare Materials* 11 (2022): 2201544, https://doi.org/10.1002/adhm.202201544.

42. C. Martins, F. Sousa, F. Araújo, and B. Sarmento, "Functionalizing PLGA and PLGA Derivatives for Drug Delivery and Tissue Regeneration Applications," *Advanced Healthcare Materials* 6 (2017): 1701035.

43. W.-Q. Cai, W. Liang, D. Li, et al., "Reactive Oxygen Species-responsive Polymer Drug Delivery System Targeted Oxidative Stressed Colon Cells to Ameliorate Colitis," *ACS Nano* 19 (2025): 17287–17308, https://doi.org/10.1021/acsnano.4c14373.

44. J. M. Blander, "Death in the Intestinal Epithelium—Basic Biology and Implications for Inflammatory Bowel Disease," *The FEBS Journal* 283 (2016): 2720–2730, https://doi.org/10.1111/febs.13771.

45. L. M. Ensign, R. Cone, and J. Hanes, "Oral Drug Delivery with Polymeric Nanoparticles: The Gastrointestinal Mucus Barriers," *Advanced Drug Delivery Reviews* 64 (2012): 557–570, https://doi.org/10.1016/j.addr.2011.12.009.

46. S. Lai, Y. Wang, and J. Hanes, "Mucus-Penetrating Nanoparticles for Drug and Gene Delivery to Mucosal Tissues," *Advanced Drug Delivery Reviews* 61 (2009): 158–171, https://doi.org/10.1016/j.addr.2008.11.002.

47. J. K. Gustafsson and M. E. V. Johansson, "The Role of Goblet Cells and Mucus in Intestinal Homeostasis," *Nature Reviews Gastroenterology & Hepatology* 19 (2022): 785–803, https://doi.org/10.1038/s41575-022-00675-x.

48. S. Citi, "Intestinal Barriers Protect Against Disease," *Science* 359 (2018): 1097–1098, https://doi.org/10.1126/science.aat0835.

49. W.-T. Kuo, L. Zuo, M. A. Odenwald, et al., "The Tight Junction Protein ZO-1 Is Dispensable for Barrier Function but Critical for Effective Mucosal Repair," *Gastroenterology* 161 (2021): 1924–1939, https://doi.org/10.1053/j.gastro.2021.08.047.

50. M. F. Neurath, "Strategies for Targeting Cytokines in Inflammatory Bowel Disease," *Nature Reviews Immunology* 24 (2024): 559–576, https://doi.org/10.1038/s41577-024-01008-6.

51. P. Xiao, Z. Hu, J. Lang, et al., "Mannose Metabolism Normalizes Gut Homeostasis by Blocking the TNF-α-mediated Proinflammatory Circuit," *Cellular & Molecular Immunology* 20 (2023): 119–130.

52. C. Danne, J. Skerniskyte, B. Marteyn, and H. Sokol, "Neutrophils: From IBD to the Gut Microbiota," *Nature Reviews Gastroenterology & Hepatology* 21 (2024): 184–197, https://doi.org/10.1038/s41575-023-00871-3.

53. C. Manichanh, N. Borruel, F. Casellas, and F. Guarner, "The Gut Microbiota in IBD," *Nature Reviews Gastroenterology & Hepatology* 9 (2012): 599–608, https://doi.org/10.1038/nrgastro.2012.152.

54. X. Tang, Y. Shang, H. Yang, et al., "Targeted Delivery of Fc-fused PD-L1 for Effective Management of Acute and Chronic Colitis," *Nature Communications* 15 (2024): 1673, https://doi.org/10.1038/s41467-024-46025-0.

55. H. Qi, Y. Li, H. Yun, et al., "Lactobacillus Maintains Healthy Gut Mucosa by Producing L-ornithine," *Communications Biology* 2 (2019): 171, https://doi.org/10.1038/s42003-019-0424-4.

56. Y. Zhu, B. Chen, X. Zhang, et al., "Exploration of the Muribaculaceae family in the Gut Microbiota: Diversity, Metabolism, and Function," *Nutrients* 16 (2024): 2660, https://doi.org/10.3390/nu16162660.

57. X. Lin, T. Hu, Z. Wu, et al., "Isolation of Potentially Novel Species Expands the Genomic and Functional Diversity of Lachnospiraceae," *iMeta* 3 (2024): 174.

58. S. Shabana, H. I. Hamouda, S. Noureldin, Z. Chi, and C. Liu, "Marine Phospholipid Nanoliposomes Mediate Oral Colonic Delivery of 5-aminosalicylic Acid and Mitigate the Severity of DSS-induced Colitis in Mouse Models," *Journal of Drug Delivery Science and Technology* 108 (2025): 106821, https://doi.org/10.1016/j.jddst.2025.106821.

59. A. Ahmad, M. M. Ansari, R. K. Mishra, et al., "Enteric-coated Gelatin Nanoparticles Mediated Oral Delivery of 5-aminosalicylic Acid Alleviates Severity of DSS-induced Ulcerative Colitis," *Materials Science and Engineering: C* 10 (2021): 111582.

60. Z. Li and Q. Yang, "Biomarker-responsive Nanomaterials for Precision Theranostics in Inflammatory Bowel Disease," *Coordination Chemistry Reviews* 552 (2026): 217467, https://doi.org/10.1016/j.ccr.2025.217467.

61. Z. Gu, Y. Dong, S. Xu, L. Wang, and Z. Liu, "Molecularly Imprinted Polymer-Based Smart Prodrug Delivery System for Specific Targeting, Prolonged Retention, and Tumor Microenvironment-Triggered Release," *Angewandte Chemie International Edition* 60 (2021): 2663–2667, https://doi.org/10.1002/anie.202012956.

62. Y. Lee, K. Sugihara, M. G. Gillilland, S. Jon, N. Kamada, and J. J. Moon, "Hyaluronic acid–bilirubin nanomedicine for targeted modulation of dysregulated intestinal barrier, microbiome and immune responses in colitis," *Nature Materials* 19 (2020): 118–126, https://doi.org/10.1038/s41563-019-0462-9.

63. Y. Li, Y. Xu, C. Pan, Z. Ren, and X. Yang, "TRIF Is Essential for the Anti-inflammatory Effects of Astragalus Polysaccharides on LPS-infected Caco2 Cells," *International Journal of Biological Macromolecules* 159 (2020): 832–838, https://doi.org/10.1016/j.ijbiomac.2020.05.005.

Supporting Information

Additional supporting information can be found online in the Supporting Information section.

Supporting File: adhm71014-sup-0001-SuppMat.pdf